Title
Regularized Equally Sloped Tomography Algorithm for Low Dose X-Ray Computed Tomography

Author
Zhao, Yunzhe

Publication Date
2012

Peer reviewed|Thesis/dissertation

UNIVERSITY OF CALIFORNIA

Los Angeles

Regularized Equally Sloped Tomography Algorithm for Low Dose X-Ray Computed Tomography

A dissertation submitted in partial satisfaction of the

requirements for the degree Doctor of Philosophy

in Physics

by

Yunzhe Zhao

2012

ABSTRACT OF THE DISSERTATION

Regularized Equally Sloped Tomography Algorithm for

Low Dose X-Ray Computed Tomography

By

Yunzhe Zhao

Doctor of Philosophy in Physics

University of California, Los Angeles, 2012

Professor Jianwei Miao, Chair

X-ray Computed Tomography is widely used in a broad range of fields including astronomy, geophysics, material science, biology and radiology. It has the advantage to achieve the cross section information of the object without physically damaging or penetrating it, which is especially important for in-vivo biology imaging systems or clinical imaging systems. However, due to the requirement of sufficiently high flux projections from multiple directions for achieving high quality images, a major concern in X-ray CT is the unavoidable radiation dose delivered to the imaging objects, especially to the more radiosensitive patients or biology specimens. With the conventional unregularized tomography algorithms, the accuracy of the reconstruction images has to be compromised by lowering the number of projections or reducing the source flux per projection. Therefore, many more sophisticated reconstruction algorithms

have been developed recently to solve the missing data and suppress the noise level in the low dose tomography modalities by incorporating mathematical regularization techniques into a real space iterative process. These methods perform well under certain circumstances but also have the limitation in computational speed, which is crucial for real time imaging systems.

In this dissertation, an efficient iterative Fourier based reconstruct technique termed Equally-Sloped Tomography (EST), which combines the efficiency of Fourier transform and advanced iterative process and allows for accurate tomographic reconstruction from low flux and undersampled projection data, is presented and investigated. This work focuses on integrating the mathematical regularization methods into the EST algorithm, studying its performances through numerical experiments, comparing the results with other reconstruction algorithms and developing the data preparation procedure for three major tomography geometries: parallel beam, fan beam and helical cone beam. Furthermore, the algorithm was implemented into two important tomography systems: the X-ray medical CT and phase contrast X-ray mammography CT. The performances were studied by conducting experiments using phantom and clinical data at different low dose levels. After carefully evaluated by both visualized comparisons and quantified measurements, the results demonstrate that the regularized EST algorithm is capable to computational efficiently achieve significant radiation dose reduction through both the reduction of flux and the number of projections, while producing comparable image quality results as the full-dose conventional reconstructions do.

The dissertation of Yunzhe Zhao is approved.

Dolores Bozovic

Henry Huang

James Rosenzweig

Jianwei Miao, Committee Chair

University of California, Los Angeles

2012

In dedication to my mother and father.

TABLE OF CONTENTS

LIST OF FIGURES

LIST OF TABLES

ACKNOWLEDGEMENTS

No words can adequately convey my gratitude to my advisor, Prof. Jianwei Miao, for his invaluable inspiring guidance, warm encouragement, great enthusiasm and constant support over the past 5 years. I will forever be thankful for having this amazing opportunity to work with him and learn from him, his mentorship will continue inspiring me to learn and grow through all my life, personal and professional. And I owe my heartfelt gratitude to my outstanding PhD committee members, Prof. Dolores Bozovic, Prof. Henry Huang, and Prof. James Rosenzweig, for their valuable suggestions, generous support throughout the dissertation process and honoring me by serving on my committee.

A portion of this work stated in Chapter 2 and 3 is a version of the article "Radiation dose reduction in X-ray CT by using a Fourier-based iterative reconstruction method". I would like to express my thanks to the co-authors for their contributions: B. Fahimian, Z. Huang, R. Fung, Y. Mao, C. Zhu, M. Khatonabadi, J. DeMarco, S. Osher, M. McNitt-Gray and J. Miao.

A portion of this work stated in Chapter 4 is a version of the article "High resolution, low dose phase contrast x-ray tomography for 3D diagnosis of human breast cancers". I would like to express my thanks to the co-authors for their contributions: E. Brun, P. Coan, Z. Huang, A. Sztrokay, P. Diemoz, S. Liebhardt, A. Mittone, S. Gasilov, J. Miao and A. Bravin.

I would also like to thank my colleagues of the Coherent Imaging Group in department of Physics at UCLA for all the continuous suggestions, discussions and over support.

I am also grateful to Physics Department at UCLA and all my good friends at UCLA for giving me an incredible graduate school experience.

Finally, I would like to extend my thanks to my parents and my husband Xiaoyang, for giving me unconditional love, bringing happiness everyday to my life and always being on my side no matter what.

VITA

2005-07	Research Assistant Hefei National Laboratory for Physical Sciences at the Microscale Hefei, Anhui, China
2007	Bachelor of Science in Physics University of Science and Technology of China Hefei, Anhui, China
2009	Master of Science in Physics University of California, Los Angeles Los Angeles, California
2007-08	Teaching Assistant Department of Physics University of California, Los Angeles
2008-09	Teaching Associate Department of Physics University of California, Los Angeles
2010-12	Graduate Student Researcher Coherent Imaging Group Department of Physics and Astronomy University of California, Los Angeles

CHAPTER 1

INTRODUCTION

Tomography is a widely used imaging method. In Greek, *totmos* means section and *graphy* means to write, and how the word is derived explains well how the method works: first obtain projections using penetrating wave, then compute an image by combining the projections. Tomographic imaging is specifically developed for revealing hidden structures that are not directly accessible. For this reason, tomographic imaging is widely used in a broad range of fields including astronomy, geophysics, material science, biology and radiology. As an example, tomographic implementations of transmission X-ray imaging modalities, such as X-ray absorption and phase contrast imaging, present important applications to biology and medicine (1-7). For instance, absorption imaging allows for tunable elemental mapping of specimens, while phase contrast imaging offers 100-1000 times increased sensitivities in the hard x-ray region relative to absorption imaging hence allows for low contrast object's imaging (1). Another example is the X-ray computed tomography (CT) which was introduced in the 1970s and has become a revolutionary medical tool in the diagnosis of a large number of diseases as well as the visualization of critical interventional procedures today (8).

With all kinds of applications and implementations, the underlying computational questions for all tomographic imaging methods are essentially the same: how to obtain projections with minimum radiation dose and what is the best way to achieve most accurate reconstruction from the projections. In real world, projections are never free of noise, and sometimes even have

missing parts. Theoretically, projections with higher signal-to-noise ratio can be obtained by using higher flux X-ray and such projections will lead to better and cleaner reconstruction, while more number of projections can provide more information and prevent the under sampled artifacts in the reconstructions. However, the limitation of device output and the potential negative impact of radiation dose imparted to biological specimens and patients in biology and radiology applications put constrains on the acquisition source flux or sample size. In biological and medical imaging, the control of high flux used for transmission tomography is of particular concern. Similar to other tomographic imaging method, transmission tomographic imaging systems reconstruct object cross-section by mathematical reconstructing projections. In order that a good cross-section is obtained, projections shall to be taken with sufficiently high flux, and from reasonable number of different directions. But a high dose can potentially impair the biological specimens and patients. For example, in vitro imaging of cells and macromolecules using transmission electron tomography, conformal changes due to radiation damage can be readily visualized if the number of projections is not limited. The concern of potential negative effect from high radiation dose is even more severe in medical imaging modality. The radiation dose from CT procedures represents the most significant source of man-made radiation to the public and disproportionally accounts for more than 70% radiation dose in medical procedures (9). The typical effective doses in medical CT procedures are one to two orders of magnitude higher than a typical chest radiograph for example, depending on the type of procedure (10). Due to the rapid increase in the popularity and frequency of CT procedures, a significant concern is the potential for radiation carcinogenesis, specifically to the more radiosensitive populations

such as pediatrics. Such concern urged the development of computed tomographic image reconstruction method that works on projections obtained from low radiation dose.

In theory, radiation dose can be reduced through two ways given a fixed energy spectrum and scanner configuration. The first way is to reduce of the number of projections while maintaining the flux in each projection. This solution relies on under-sampling the number of tomographic projections, which is capable of simultaneously reducing both the acquisition time and radiation dose. But conventional reconstruction algorithms are not able to reconstruct accurate results due to the violation of Nyquist sampling criteria. The tomographic reconstruction in undersampling condition faces an ill-imposed problem due to the missing projection information. It was demonstrated that reduced number of projections adversely affects the accuracy of reconstructions (11). In coherent diffraction microscopy imaging studies where missing information problem is also encountered due to missing phase data of the diffraction recordings, previous works proved that iterative oversampling Fourier methods is capable of solving for missing information under noisy conditions for noncrystaline and nanocrystal samples (12-15). In this dissertation, such method was developed and applied to aid the recovery missing information in low dose X-ray tomography reconstruction. More specifically, an exact Fourier based oversampling method for tomographic reconstruction, termed Equally-Sloped Tomography (EST), was developed and investigated to solve the missing data problem due to undersampled projections. EST is an iterative Fourier based reconstruction that combines the exactness of the exact and novel Fourier transform, the physical and mathematical constraints, the oversampling method and the strictly measurement enforcement(16-18). In this dissertation,

it will be demonstrated that EST is capable of reconstructing better image less number of projections without sacrificing the image quality. The algorithm was implemented and evaluated on the synchrotron X-ray phase contrast mammography CT system at European Synchrotron Radiation Facility (ESRF) in France. A human breast sample with breast cancer was imaged with 2000 projections and the reconstructions were performed by manually removing the number of projections from 2000 to 200, which is only one tenth of the original projections and radiation dose. The reconstruction results were evaluated by both quantitative measurements, visualization comparison with conventional Filtered-Back Projection (FBP) reconstruction algorithms and blind evaluation by five independent radiologists. It is been proved that, our advanced EST algorithm can reduce the radiation dose and acquisition time by ~74% relative to conventional phase contrast x-ray tomography, while maintaining high image resolution and image contrast. As large-scale and compact synchrotron radiation facilities are currently under rapid development worldwide, the implementation of the advanced EST reconstruction algorithm into low dose X-ray phase-contrast CT could find broad applications in biology and medicine fields.

The second way to reduce the radiation dose, on the other hand, is to reduce the flux of source. Previous work suggested that reducing the radiation dose by lower the flux leads to a significant degradation of resolution, low contrast visibility, and geometrical fidelity due to the increasing noise level (8, 19). So in this low flux and high noise conditions, we incorporated advanced mathematical regularization constraints into our EST algorithm to suppress the noise on reconstructed images, such as the Total Variation (TV) (20) and Non Local Total Variation (NLTV) (21) regularization techniques. A series of numerical experiments were conducted in

this thesis, different levels of Poisson noise were added to the projections and the regularized EST algorithm results were compared with both conventional FBP algorithm and the newly developed regularized iterative algebraic and statistics reconstruction algorithms such as ART and EM (19). The numerical results indicate that the regularized EST algorithm can efficiently remove the noise on the reconstructed image without the compromise of image quality and computational time. Furthermore, the regularized EST algorithm was extended to fan beam, helical cone beam geometries and them implemented onto to the clinical Siemens SOMOTOM Sensation 64 medical CT scanner. The EMMA phantom and clinical pediatric patient data was collected and the reconstruction performance at different flux levels were evaluated from the perspective of resolution, contrast ,shape fidelity and noise level with the quantification metrics such as Signal to Noise Ratio (SNR) and Contrast to Noise Ratio (CNR). The result indicate that since the radiation dose is linearly proportional to the X-ray flux, in this case, the regularized EST algorithm enable a reduction of the CT dose by about 70% without compromising the image quality and accuracy compared to the conventional FBP reconstruction method. The regularization techniques can help the EST iterative process to suppress the noise while the iterative process can always keep the result consistent with the measurement and prevent the regularization step removing the fine structures from the image. This is to say, the regularized EST algorithm is an efficiency reconstruction method to remove the image noise in the low flux X-ray tomography modalities.

To summarize, a regularized EST iterative reconstruction algorithm is developed and described in this dissertation, which is capable of producing accurate reconstructions in the low radiation

dose tomography conditions, such as using less number of projections or using the projections obtained through low radiation dose flux. This new EST reconstruction algorithm provides a promising solution to reduce the negative effects on biological specimens and the potential risk of harm on patients taking X-ray tomography imaging. This thesis will describe the theoretical background, algorithm development, numerical experiment, real system implementation, and performance evaluation of the proposed acquisition and reconstruction method. In the study of the new EST algorithm's application in synchrotron X-ray phase contrast tomography set up and medical X-ray CT scanner, a series of image quality studies on phantoms, human breast cancer sample and clinical pediatric patient data sets at various simulated dose levels were used. We quantitatively assessed the performance of this regularized EST algorithm and compared it to the existing reconstruction methods. To quantify the potential for dose reduction from this new method, we measured across a series of image quality metrics the factor by which the number of projections or the source flux can be reduced while still achieving comparable results relative to conventional reconstruction at full dose. In the study of phase contrast X-ray mammography CT with the human breast sample, a ~74% dose reduction can be achieved while in the study of medical X-ray CT scanner, a potential radiation dose reduction in the range of 65-80% was observed by using the proposed EST reconstruction algorithm.

References

1. P. Cloetens *et al.*, "Hard x-ray phase imaging using simple propagation of a coherent synchrotron radiation beam". J. Phys. D: Appl. Phys., 32, p. A145-A151 (1999).
2. M. Langer, *et al.*, "Quantitative comparison of direct phase retrieval algorithms in in-line phase tomography". Med Phys, **35**(10): p. 4556-66(2008).
3. A. Momose, et *al.*, "Phase-contrast X-ray computed tomography for observing biological soft tissues", Nat Med, **2**(4): p. 473-475(1996).
4. K. A. Nugent, *et al.*, "Quantitative Phase Imaging Using Hard X Rays. Phys.Rev.Lett", **77**(14): p. 2961(1996).
5. M. Bech, *et al.*, "Hard X-ray phase-contrast imaging with the Compact Light Source based on inverse Compton X-rays". J Synchrotron Radiat. 16(Pt 1): p. 43-7(2009).
6. T. Weitkamp, *et al.*, "X-ray phase radiography and tomography of soft tissue using grating interferometry". Eur J Radiol, **68**(3 Suppl): p. S13-7(2008).
7. D.M. Connor, *et al.*, "Comparison of diffraction-enhanced computed tomography and monochromatic synchrotron radiation computed tomography of human trabecular bone". Phys Med Biol, **54**(20): p. 6123-33(2009).
8. J.T Bushberg, "The essential physics of medical imaging". 2nd ed. 2002, Philadelphia: Lippincott Williams & Wilkins. xvi, p.933.
9. National Research Council (U.S.). Committee to Assess Health Risks from Exposure to Low Level of Ionizing Radiation., Health risks from exposure to low levels of ionizing

radiation: BEIR VII Phase 2. 2006, Washington, D.C.: National Academies Press. xvi, 406 p.

10. A. J. Einstein, M. J. Henzlova and S. Rajagopalan, "Estimating risk of cancer associated with radiation exposure from 64-slice computed tomography coronary angiography. JAMA. **298**(3): p. 317-23(2007).
11. E. Lee, et *al.,* "Radiation dose reduction and image enhancement in biological imaging through equally-sloped tomography. J. Struc. Bio. 2008.
12. J. Miao, *et al*., "Extending the methodology of X-ray crystallography to allow imaging of micrometre-sized non-crystalline specimens". Nature. **400**: p. 342-344(1999).
13. K. S. Raines, et *al*., "Three-dimensional structure determination from a single view". Nature, **463**(7278): p. 214-217(2010).
14. M. A. Pfeifer, *et al*., "Three-dimensional mapping of a deformation field inside a nanocrystal. Nature, **442**(7098): p. 63-6(2006).
15. B. Abbey, *et al*., "Keyhole coherent diffractive imaging". Nat Phys. 4(5): p. 394-398(2008).
16. J. Miao, F. Föster and O. Levi. "Equally sloped tomography with oversampling reconstruction", Phys. Rev. B, **72**, 052103(2005).
17. B. P. Fahimian, Y. Mao, P. Cloetens and J. Miao, "Low dose X-ray phase-contrast and absorption CT using equally-sloped tomography". Phys. Med. Biol, **55:** p. 5383-5400(2010).

18. Scott, M. C. *et al*. “Electron tomography at 2.4 Ångstrom resolutions”. Nature **483**, p.444-447(2012).
19. A. C. Kak and M. Slaney, Principles of Computerized Tomographic Imaging. 2001: SIAM.
20. L.I, Rudin, S. Osher, and E. Fatemi, “Nonlinear total variation based noise removal algorithms”. Physica D, 60, p.259-268(1992).
21. G. Gilboa and S. Osher, “Nonlocal operators with applications to image processing,” Multiscale Model. Simul. **7**, p.1005–1028 (2008).

CHAPTER 2

REGULARIZED EQUALLY SLOPED TOMOGRAPHY ALGORITHM

2.1. Introduction

Transmission tomography technique has been recognized as one of the most widely used methods to reconstruct the cross-section of objects. It has broad applications in different fields such as in-vivo biology images and clinical medical systems. However, due to the requirement of multiple projections taken from different angles at high flux setting for accurate tomography, it is inherently a high radiation dose imaging technique. There are two direct ways to reduce radiation dose in tomography modalities, one is to reduce the number of acquisition projections, and the other is to reduce the source flux for per projection. But for the conventional Filtered-Back Projection (FBP) reconstruction algorithm, the former way would cause the sampled projections not satisfy the Nyquist sampling requirement, while the latter option will introduce heavier noise to the image then degrade the reconstructed image quality (1, 2). Therefore, how to compromise between low radiation dose and high reconstructed image accuracy has been a challenge for conventional tomography algorithms. Accordingly, many advanced iterative algorithms have been developed recently trying to use the portion of data to recover the missing data or incorporate the mathematical regularization into the iterative process to guide the image to a less noisy stage (3-10). Though these methods perform well under certain circumstances, because of

the limitations mainly in computation speed, currently the most popular method in tomographic field remains FBP and its variations (11).

In 2005, a Fourier-based iterative method, denoted equally sloped tomography (EST) was developed to allow the 3D image reconstruction from a limited number of projections. It has been demonstrated that EST is an effective method for significant reduction of radiation dose in several tomographic applications, including transmission electron tomography, X-ray diffraction microscopy, and synchrotron based X-ray phase contrast and transmission CT (12-17). More recently, it has been proved that EST can be used for 3D structure determination of nanomaterials at atomic scale resolution (18) as well as for high resolution, low dose phase contrast X-ray imaging of human breast cancers in three dimensions (19). Previous works on EST are mainly focus on maintaining the reconstructed image quality while reducing the number of projections. In this chapter, we incorporate advance mathematical regularization technique into the EST algorithm, and after the introduction to the conventional FBP algorithm and iterative reconstruction algorithms such as ART and EM, our Fourier based regularized EST iterative algorithm is explained in details with simulation results and compared with other reconstruction algorithms. At the end, the implementation of EST algorithm for three most widely used tomography geometries: parallel beam, fan beam and helical cone beam were achieved in the simulation stage.

2.2 Computed Tomography Reconstruction Theory and Algorithms

2.2.1. Fourier Slice Theorem

The foundation of tomography is Fourier Slice Theory. It makes possible for the transformation from the object space image projections to the Fourier space image information. The theory states that the 1D Fourier transform of a parallel geometry projection $P_\theta(t)$ at angle θ gives the value of the 2D Fourier transform of the reconstructed image at the same angle (1). Eq. 2.1 shows the simplest case when $\theta = 0$:

$$\int_{-\infty}^{\infty} P_0(t) e^{-j2\pi\omega t} dt = \int_{-\infty}^{\infty} \left[\int_{-\infty}^{\infty} f(x,y) e^{-j2\pi ux} dy \right] dx \qquad (Eq. 2.1)$$

In Eq. 2.1, t is the distance of the each point on the detector from the center of detector, *f(x,y)* is the reconstructed image. Fig. 2.1 shows the scheme of Fourier Slice Theorem.

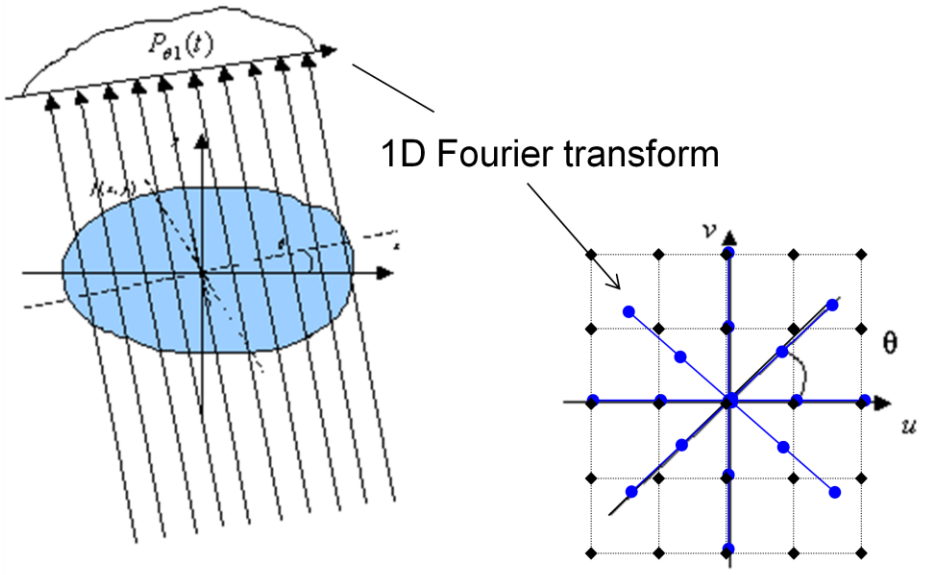

Figure 2.1. Illustration of the Fourier Slice Theorem. It states that 1D Fourier transform of a parallel geometry projection $P_\theta(t)$ at angle θ gives the value of the 2D Fourier transform of the reconstructed image at the same angle

Using the Fourier Slice Theorem, the direct algorithm to reconstruct image from measured projections has two steps. First, perform a 1D Fourier transform to transform the measured projections to the points in the Fourier spaces. The second step is to perform an inverse 2D FFT on the Fourier space points then achieve the image in the real space. Since the data is acquired along equally increase angles, the value set has a polar grid distribution in the Fourier space. The implementation difficulty for this direct method is that, there is no exact Fourier transform between polar grid in Fourier space and Cartesian grid in image space (20-22). So before the inverse 2D FFT, a regridding step is required to interpolate the points from polar grid to

Cartesian grid in Fourier space. Unlike the interpolation in object domain, in which the error is constraint to a local region, each point in Fourier space correspond to the whole image in object space and the interpolation error may degrade the quality of the whole image.

2.2.2. Filtered Back Projection Reconstruction Algorithm

Because of the regridding requirement in the direct Fourier method, nowadays, the most popular reconstruction algorithm in CT systems is Filtered-Back Projections (FBP). It was independently developed by Bracewell et.al in 1967 (23) and Ramachandran et.al in 1971(24). The basic idea of back-projection is to retrieve the image by simply back projecting the measured projections, smearing the values in the direction from where the radiation beam came. But as the measured projections are distributed on polar grid in Fourier space as the blue lines in Fig.1, the low frequency grid points are distributed denser than the high frequency points away from the center. If the measured projections are used directly for back-projection, the low frequency information will be over emphasized compared to the high frequency information and cause the blur on the edge and fine structures. To overcome this issue, the projections in Fourier domain will multiply a necessary high-pass filter before the back-projection step, which gives the term "Filtered" in FBP algorithm. The most common high-pass filter used in FBP $|q|$ is linearly increased with the frequency variation and is called Ramp-Like filter. The FBP algorithm can be expressed by Eq. 2.2, in which N is the number of total projections, $\boldsymbol{\mathcal{F}}_n(u)$ is the 1D Fourier transform of the n^{th} projection.

$$f(x,y) = \sum_{n=0}^{N} \int_{0}^{\infty} \mathcal{F}_n(u)\,|q| e^{j2\pi w} d \qquad (Eq.\,2.2)$$

FBP has the advantage of fast computational speed, easy implementation and its independency of parameter adjustment. However, a good FBP reconstruction requires large number of less-noisy projections. This is the mainly drawback since the newly developed tomography systems try to further reduce the radiation dose by reducing either the number of projections or the flux from source. In these conditions, The FBP algorithm is a one step process without any feed- back system and lacks the flexibility as the advanced iterative algorithms do.

2. 2. 3. Iterative Algebraic and Statistical reconstruction algorithms

For the low dose tomography systems, algebraic and statistical iterative reconstruction methods could be served as alternatives methods. Actually, the first CT image was reconstructed by the algebraic reconstruction techniques (ART). Unlike the FBP algorithm which simply smears the filtered projections back to retrieve the reconstruction images, the iterative algorithms work as searching the most fitted solution by applying constraints in each iteration. The most widely used methods are algebraic reconstruction techniques (ART) and statistical reconstruction techniques such as Expectation Maximization method (EM). Fig. 2.2 shows the idea and scheme of ART algorithm (1), which can be considered as solving a set of linear equations through an iterative approach. Fig. 2.2 (a) shows the idea of that, in the tomography imaging system, for each ray, it can be presented as a linear equation of the sum of all the pixels that it goes through. So the set

of linear equations in Fig. 2.2 (a) can be written as Eq. 2.3. For this simple 2 x 2 system, there are 4 unknown values $f_1 \sim f_4$ and 8 linear equations. Since the number of equations is larger than the number of unknown values in this case, the unknowns can be calculated easily with the equations.

$$\begin{matrix} f_1 = S_1 \\ f_2 + f_3 = S_2 \\ f_4 = S_3 \end{matrix} \qquad \begin{matrix} f_3 = S_4 \\ f_1 + f_4 = S_5 \\ f_2 = S_6 \end{matrix} \qquad \begin{matrix} f_3 + f_4 = S_7 \\ f_1 + f_2 = S_8 \end{matrix} \qquad (Eq.\,2.3)$$

In the ART method implemented for the real tomography system as shown in Fig. 2.2 (b), the width of the X-ray beam $\Delta\xi$ is taken into account, then each projection can be viewed as an area weighting sum of all the pixels that it goes through. Eq. 2.4 expresses the equation for this system in which the area weight a_{ij} is between the interval of 0 and 1.

$$a_{ij} = \frac{illuminated\ area\ of\ pixel\ j\ by\ beam\ i}{total\ area\ of\ pixel\ j} \qquad (Eq.\,2.4)$$

$$\sum_{j=1}^{N} a_{ij} f_j = P_i$$

And in the real tomography systems, the unknown values are of ~ 10^6, while the number of projection equations can be as many as 10^6. So it is almost impossible to solve the equation set by a directly matrix inversion. Therefore, in ART algorithm, instead of direct matrix computation, the resolution is approached iteratively as Eq. 2.5.

$$f_j^{(n)} = f_j^{(n-1)} + \frac{p_n - q_n}{\sum_{i=1}^{N} a_{ij}^2} a_{ij}$$
$$q_n = \sum_{i=1}^{N} f_i^{(n-1)} a_{ij} \qquad (Eq. 2.5)$$

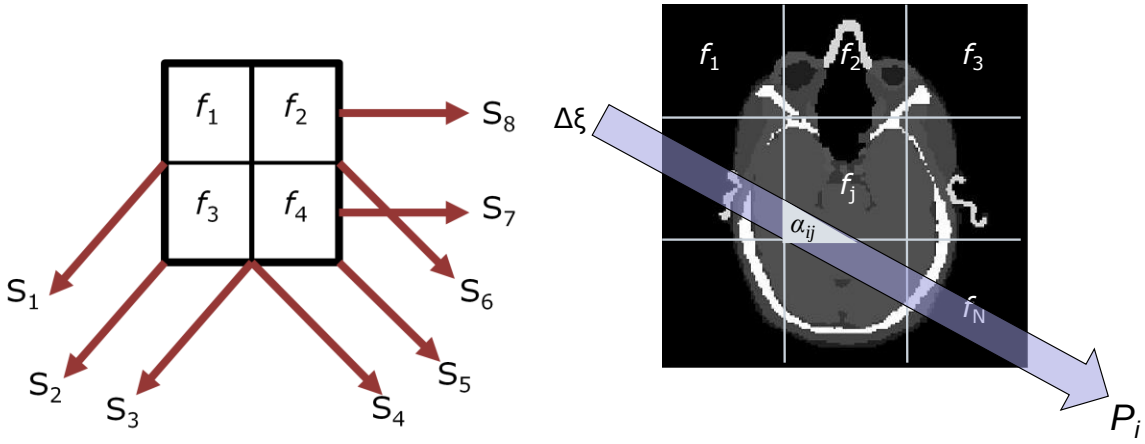

(a) (b)

Figure 2.2. Schematic for ART iterative reconstruction algorithm. (a) The basic idea is to solve the image pixels as several unknowns while taking the projections as multiple independent linear integral equations. There are 4 unknowns and 8 linear equations in the example with a size of 2 x 2. (b) ART takes into account the width of each ray, so each point in the projection is an area weighting sum of all the pixels that it goes through. For example, the weighting of the projection P_i goes through the pixel f_j is a_{ij}.

One drawback of the ART algorithm is that, as it takes the measured projections as "ground truth" and always tries to match the measurements with reconstruction, when the source flux is low and the projections are noisy, the reconstructed images will be noisy as well. In this kind of low dose tomography condition, statistical reconstruction algorithm such as EM is more suitable

since it incorporate the noise model into the algorithm. The EM algorithm for the transmission tomography iterates between an expectation (E) step, which creates the expectation function using the estimated reconstructed image, measured projections and Poisson noise model, and the maximization (M) step, which computes the next generation of the reconstructed image to maximize the expected log-likelihood function established in the E step (25). The algorithm can be expressed as Eq. 2.6, in which N is the total number of voxels to be reconstructed, each voxel has a constant attenuation factor f_j . b_i is the i[th] measured projections, M is the number of total projections and A is the discrete Radon transform, n is the index for current iteration number.

$$f_j^{(n)} = \frac{\sum_{i=1}^{M}\left(a_{ij}\left(\frac{b_i}{(Af^{(n-1)})_i}\right)\right)}{\sum_{i=1}^{M} a_{ij}} f_j^{(n-1)} \quad , j = 1, \ldots . N. \qquad (Eq. 2.6)$$

Both the algebraic and statistical reconstruction techniques have the advantage that they are flexible to incorporate constraints, such as mathematical regularization methods or some physical constraints. This benefits most for the low dose radiation CT protocols, when the sample set (number of projections) is very low or the noise level is high. But compared to FBP algorithm or Fourier based methods, these real space iterative algorithms have high computational complexity that keeps them away from widely implementation in the tomography systems especially for clinical CT systems.

2.3. Regularized Equally Sloped Tomography

2.3.1. Pseudo-Polar Fast Fourier Transfer (PPFFT)

From Fourier slice theory, we can learn that in theory if infinity projections are acquired around the object, after one 1D Fourier transform and one 2D inverse FFT the reconstructed image can be achieved. But in the real acquisition progress, the number of projections can be acquired is limited and the equally angle acquisition method would always result in a polar grid distribution in the Fourier space. Since there is no exact Fourier transform between polar grid in Fourier space and Cartesian grid in object space an interpolation step is required in the Fourier space before the inverse FFT step. There are several approaches for the interpolation in Fourier space, such as the typical interpolation schemes like nearest neighboring, linear, cubic or the more advanced and accurate method include non-uniform FFT (NUFFT) (20-21,26-27) . But unlike the interpolation in object domain, in which the error is restricted to a local area, each point in Fourier space correspond to the whole image in object space and the interpolation error may degrade the quality of the whole image. Luckily, if we acquire the projections not along the equally increase angels, but along the equally increase slopes, there exists a direct and exact fast Fourier transform termed pseudo-polar fast Fourier transform(PPFFT) between the pseudo-polar grid in Fourier domain and the Cartesian grid in the object domain (28,29). As shown in Fig. 2.3, for an N x N Cartesian grid, the pseudo-polar grid is defined by a set of 2N lines, each line consisting of 2N grid points mapped out on N concentric squares. The 2*N* lines are subdivided into two groups: a horizontal group (in blue) defined by y = s*x and a vertical group (in red)

defined by x = s*y, in both equations s represents the slope and |s|≤ 1. These pseudo-polar lines are termed "equally-sloped" since the successive lines in both groups change by an equal sloped increment as opposed to a fixed equal angled increment as in the polar grid. This pseudo-polar grid consists with "concentric squares", which is geometrically more close to the Cartesian grid then the polar grid's "concentric circles" distribution. And unlike the polar grid, the distance between sampling points on the individual lines of the pseudo-polar grid varies from line to line. So the fractional Fourier transform (FrFT) is necessary here to replace the conventional Fourier transform when calculating the vary output sampling distance in the Fourier domain (30). The 1D FrFT is defined as:

$$F_\alpha(k) = \sum_{X=0}^{N-1} f(x)\exp\left(-\frac{i2\pi\alpha kx}{N}\right) \qquad \alpha = \begin{cases} \frac{1}{\cos(\theta)} & Horizontal\ Set \\ \frac{1}{\sin(\theta)} & Vertical\ Set \end{cases} \qquad (Eq.2.7)$$

In Eq. 2.7, $F_\alpha(k)$ is the 1D FrFFT, $f(x)$ is the 1D tomographic projection, k and x are the coordinates in Fourier and object space, and α is the parameter that determines the distance between the sampling points in each of the 2N lines. When α = 1, the FrFFT converts to a regular FFT, while when α = -1, the FrFFT converts to a regular inverse FFT. By varying the value of α for the equally-sloped acquired projections, the Fourier space data on the pseudo-polar grids can be calculated. The pseudo-polar grid was proposed in 1974 (28) but the mathematical proved exact PPFFT and inverse PPFFT algorithms weren't developed until recently in 2004 (29). Originally the algorithm was developed to interpolate tomographic projections from the polar to the Cartesian grid in reciprocal space. And the idea of equally slope increment data acquisition

method and then incorporate the pseudo-polar grid and PPFFT into iterative algorithms for tomographic reconstructions was first proposed by Miao *et al*. in 2005 (12).

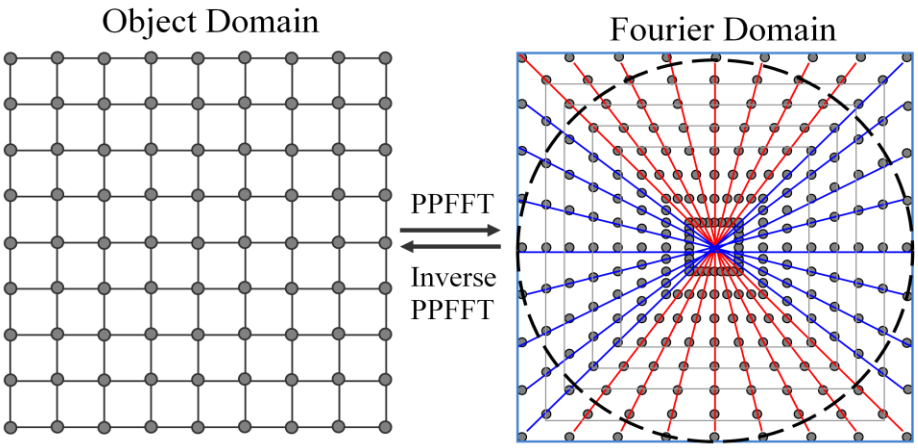

Figure 2.3. Pseudo Polar grid and PPFFT. It shows the transformation between Object domain in Cartesian grids and Fourier Domain in pseudo-polar grids. PPFFT and inverse PPFFT are exact ways to perform Fourier transform between these two domains. The dashed line indicates the resolution circle.

2.3.2. Equally Sloped Tomography Iterative reconstruction

Only the exactness of PPFFT and inverse PPFFT cannot provide all the information needed for direct reconstruction. There are three main reasons for this. First, knowledge of 2N data points along the 2N equally-sloped lines is needed to fully occupy the pseudo-polar grid and accurately invert the Fourier data using PPFFT (29). This requires a large number of projections and is not

desirable in practical applications. Secondly, the pseudo-polar grid points outside the resolution circle (indicated by the dotted circle in Fig. 2.3) cannot be experimentally obtained so there are always part of the points on pseudo-polar grid are unknown. Third, the real measurements are always with noise, especially for the low radiation dose tomography protocols. Because of all these reasons, an iterative algorithm is necessary to recover the missing data and minimize the noise of the reconstructed image through regularization. In a manner similar to the oversampling Fourier algorithm that was used to solve the phase problem in diffraction imaging (31,32), we developed the regularized Equally-Sloped Tomography (EST) iterative reconstruction algorithm, which iterates between object space and the oversampled Fourier space, with physical and mathematical constraints enforced in each iteration.

The EST algorithm is initialized by padding zeros on both sides of the projections, followed by a 1D FrFT to map the projections onto the corresponding lines in the pseudo-polar grid. The oversampling is achieved by surrounding the object in real space by mathematical zeros, a region we called 'support' and utilized as constraints in the object space. These zeros do not provide any extra information about the object itself, but they provide additional constraints in the real space and can extract more correlated information among different projections in Fourier space during the iterative process. For the equally sloped lines that have no measurements or the points on the grid outside the resolutions, the initial values are set to be zero. The j^{th} iteration of the algorithm can then be considered as the following 5 steps: (i), apply the adjoint transform to the Fourier-space slices $F_j(\vec{k})$, and obtain an real-space image, $f_j(\vec{r})$. Here we use the adjoint PPFFT to replace inverse PPFFT since the former is implemented without the conjugate gradient

method used to calculate inverse PPFFT and therefore can be computed much faster without compromising the accuracy (15) . (ii), a new object $f_j^r(\vec{r})$ is derived by enforced the mathematical regularization on $f_j(\vec{r})$. EST provides a platform that can easily incorporate any real or Fourier space regularization methods. The way to apply mathematical regularization could be very flexible, the frequency, the strength and the method of the regularization can be chosen based on different tomography modalities or imaging objects. (iii), is enforcing support and positivity constraints on $f_j^r(\vec{r})$ to achieve $f_j^{'}(\vec{r})$. Here the support S is determined based on the zero padding of the projections to achieve oversampling. The points outside the support are set to zeros as a constraint. Inside the support, all the negative values are set to zeros as a positivity physical constraint. Eq. 2.8 shows the equation of the enforcement of support and positivity constraint:

$$f_j^{'}(\vec{r}) = \begin{cases} f_j^r(\vec{r}) & \text{if } \vec{r}\,! \in \mathrm{S} \text{ or } f_j^r(\vec{r}) > 0 \\ 0 & \text{if } \vec{r} \in \mathrm{S} \text{ or } f_j^r(\vec{r}) < 0 \end{cases} \qquad (Eq.\,2.8)$$

(iv), Apply the PPFFT to $f_j^{'}(\vec{r})$ and obtain updated Fourier-space slices, $F_j^{'}(\vec{k})$. (v) Updating the Fourier-space slices by replacing $F_j^{'}(\vec{k})$ with the measured Fourier slices. The Fourier domain values outside the resolution circle and on the missing Fourier slices are remaining unchanged. The iterations are monitored by the error metric as Eq. 2.9, where $F(\vec{k})$ represents

the measured Fourier slices, $F_j^{'}(\vec{k})$ is the calculated Fourier slices in the j[th] iteration, and *R* is the radius of the resolution circle.

$$Error = \frac{\sum_k \left| F_j^{'}(\vec{k}) - F(\vec{k}) \right|_{k \le R}}{\sum_k \left| F_j^{'}(\vec{k}) + F(\vec{k}) \right|_{k \le R}} \qquad \textit{(Eq. 2.9)}$$

The algorithm then is automatically terminated when the error reach a stable stage. It normally takes about 20 iterations, depends on the tomography modality and the regularization method.

2.3.3. Mathematical Regularizations

One advantage of EST algorithm is that the prior information or regularization methods can be easily inserted and applied on the reconstructed image. Lower the source flux can reduce the radiation dose, but it will concurrently increase the noise. Many regularization methods have been developed in the field of image processing and could be implemented in reconstruction algorithms. However, most of the mathematical regularization methods require the properly chosen of one or more parameters to optimize the regularization result. For one step back projection FBP algorithm, the reconstruction result could be very sensitive to the parameters since there is no feedback after the regularization is applied, which means, even if the image is over-smoothed, the error cannot be corrected after the reconstruction. As a contrast, the EST algorithm provides a platform so that the regularization methods can be easily inserted, and its iterative process provides a feedback loop to control the strength of regularization. Even when

the reconstructed image is over-smoothed and has some patch artifacts generated by the regularization in the object domain, when the algorithm iterates back to Fourier domain, the measured projections are enforced which can prevent the spreading of artifact. The EST algorithm is always searching for a solution which is a balance between minimized noise level and measured data fidelity. In our study, we first implemented and studied the advanced regularization method termed Total Variation (TV), which is introduced by Rudin, Osher and Fatemi (33). TV method regularizes the image by minimizing the total variation of the image $f(\boldsymbol{r})$ over a domain Ω as shown in Eq. 2.10:

$$TV(f(\boldsymbol{r}) = \int_{\Omega} |\nabla f(\boldsymbol{r})| dr^3 \qquad (Eq. 2.10)$$

After incorporating the data fidelity term, the whole TV regularization process is performed by minimizing the standard TV denoising model in Eq. 2.11. TV is a nonlinear imaging denoising technique that has been widely used to remove the noise and other small artifacts while preserving sharp edges in the image. P and P^T are the forward and backward projectors, y is the measured projection. The strength or TV regularization is controlled by adjusting parameter λ, when λ is getting smaller, the TV term has more weight and the regularization strength is stronger.

$$\begin{cases} v_j(\boldsymbol{r}) = f_j(\boldsymbol{r}) - \tau P^T\left(P f_j(\boldsymbol{r}) - y\right) \\ f_{j+1}(\boldsymbol{r}) = argmin(TV\left(f(\boldsymbol{r})\right) + \frac{\lambda}{2}\left\|f(\boldsymbol{r}) - v_j(\boldsymbol{r})\right\|_2^2)) \end{cases} \qquad (Eq. 2.11)$$

In the EST algorithm, the TV regularization method can suppress noise while preserving the sharp edge if the parameter is properly chosen.

2.3.4. Data Preparation for Various Acquisition Geometries

According to the formation of Fourier slice theorem, to achieve the data on one line at a specific angle in Fourier slice, 1D Fourier transform needs to be performed on the 1D parallel projection values along the same angle. As a result, to directly utilize the information in Fourier based reconstruction algorithm such as EST, the input projection data must be in the parallel beam geometry (27). However, in the modern tomography systems, especially in medical CT systems, 2D fan-beam geometry or 3D cone-beam geometry are also utilized to increase the data acquisition efficiency. So we also developed the data preparation process to transform the data measured in fan beam or helical cone beam geometry adaptive for EST algorithm. For fan beam geometry, we utilized the common rebinning method before reconstruction, which was implemented by two 1D interpolations (34) that can transform the fan beam geometry data to parallel beam geometry that along the equally-sloped angels. The relation of the coordinates between a ray in the fan beam geometry $p(\theta, \psi)$ and a ray in the parallel geometry $p(\phi, \xi)$ is defined in Eq. 2.12, where θ is the projection angle in the fan beam geometry, ψ is the fan angle of the ray, ϕ is the projection angle in the parallel beam geometry, ξ is the perpendicular distance from the pixel position to the origin, and D is the distance from source to rotation center.

$$\begin{cases} \phi = \theta + \psi \\ \psi = \arcsin\left(\frac{\xi}{D}\right) \end{cases} \qquad (Eq. 2.12)$$

The rebinning and reconstruction for helical cone beam geometry requires more sophisticated steps. We implemented the Advanced Single-Slice Rebinning (ASSR) method (35), which is an effective algorithm that uses virtual tilted reconstruction planes along a helical path to Z-interpolate the images onto a Cartesian grid. The key step in ASSR is to rebin the helical cone-beam data into a series of 2D projections along virtual tilted planes that can be reconstructed by using conventional 2D FBP. In our implementation, we first used ASSR to rebin the helical cone-beam projections into a series of tilted slices along a helical path. Each tilt slice was reconstructed by EST and the series of 2D reconstructions was then interpolated along the Z axis to obtain a 3D image. The rebinning steps for fan-beam or cone beam geometry generate some interpolation error, but since a large number of projections were utilized in most conventional tomography system, the rebinning error could be restricted to a small value.

2.4. Numerical experiments

To evaluate the performance of EST algorithm and compared the results with conventional FBP reconstruction algorithm in the low dose tomography conditions, we designed and conducted a series of numerical experiments using the 160 x 160 pixels Zubal phantom, which was a

segmented head phantom based upon the high resolution scans of a human (36). The simulated detector has a width of 512 pixels and a total of 180 projections were calculated using a precise Fourier based discrete Radon transform (37) followed the equally- angle acquisition for FBP) or equally-sloped acquisition (for EST). To evaluate the algorithms performance under low dose tomography conditions, the Poisson noise with different flux levels ($7.0x10^5$ m^{-2} and $7.0x10^4$ m^{-2}) was added to the calculated noise-free projections. The Total Variation regularization methods were implemented into EST algorithm. The parameter is optimized for each noise level and fixed for both EST and FBP reconstructions. The FBP reconstruction was performed with the high resolution preserved un-cropped Ramp-Like filter and precise cubic interpolation.

The comparisons of the reconstruction quality and computation time among the numerical experiments of the regularized EST reconstruction algorithm, TV regularized FBP, TV base ART and TV based EM. The experiment was conducted for fan-beam geometry CT data using a 256 x 256 2D Shepp-Logan phantom with the detector size of 512 pixels and a total of 360 projections were acquired along equally increment angels. A fan to parallel rebinning step with two 1D cubic interpolations was performed for EST reconstruction input. For the FBP reconstructions, the un-cropped Ramp-Like filter was used to preserve high resolution information and the TV regularization was performed directly onto the reconstructed image. For the iterative reconstruction algorithms TV-ART and TV-EM, the TV regularization was applied in an alternative way every iteration on the current image (38, 39). For a fair comparison, all the iterative algorithms used the same number of iterations, the same rectangular support and the positive constraint. The computational time for each algorithm was recorded for computation

speed comparison. A numerical experiment for 3D helical cone beam EST reconstruction was also performed with a 3D Shepp-Logan phantom. Table 1 shows the parameters used to generate the helical cone beam data. The comparison reconstruction was performed by the conventional FDK method (40) and conventional ASSR method (35).

Detector type	Cylindrical
Detector row	64
Detector column	512
Pixel width	0.78 mm
Pixel height	0.78 mm
Distance from the source to the detector	1005 mm
Distance from the source to the center	570 mm
The helical pitch	1.4
Total projections in each circle	720

Table 2.1. Simulation parameters used for the helical cone beam CT numerical experiment. The support of the 3D Shepp–Logan phantom is an ellipsoid with half axes of 69 mm, 92 mm and 90 mm along the x- y- and z-axes, respectively. The size of reconstructed images is 512 x 512 pixels.

2.5. Results

We firstly performed the conventional FBP reconstruction on the Zubal phantom with various numbers of simulated projections. Fig. 2.4 (1-e) shows the FBP reconstruction results with 1, 4, 45, 90 and 360 projections, respectively. This series of images show that the idea of FBP is to smear the values in the direction from where the radiation beam came. So a certain number of projections are needed to reconstruct the image or there will be severe streaking artifacts on the images. Fig. 2.4 (f) is the reconstructed image from a simple back projection without any high pass filter in the Fourier space as Fig. 2.4 (e) did, so it proves that because of the imbalance of low and high frequency information in the Fourier domain, a filtered is needed to preserve the edge or details in the image. Fig. 2.4 also indicates that, since conventional FBP is a one step reconstruction algorithm without regularization, the artifacts or noise causing by low dose tomography conditions cannot be corrected and will affect the whole image quality.

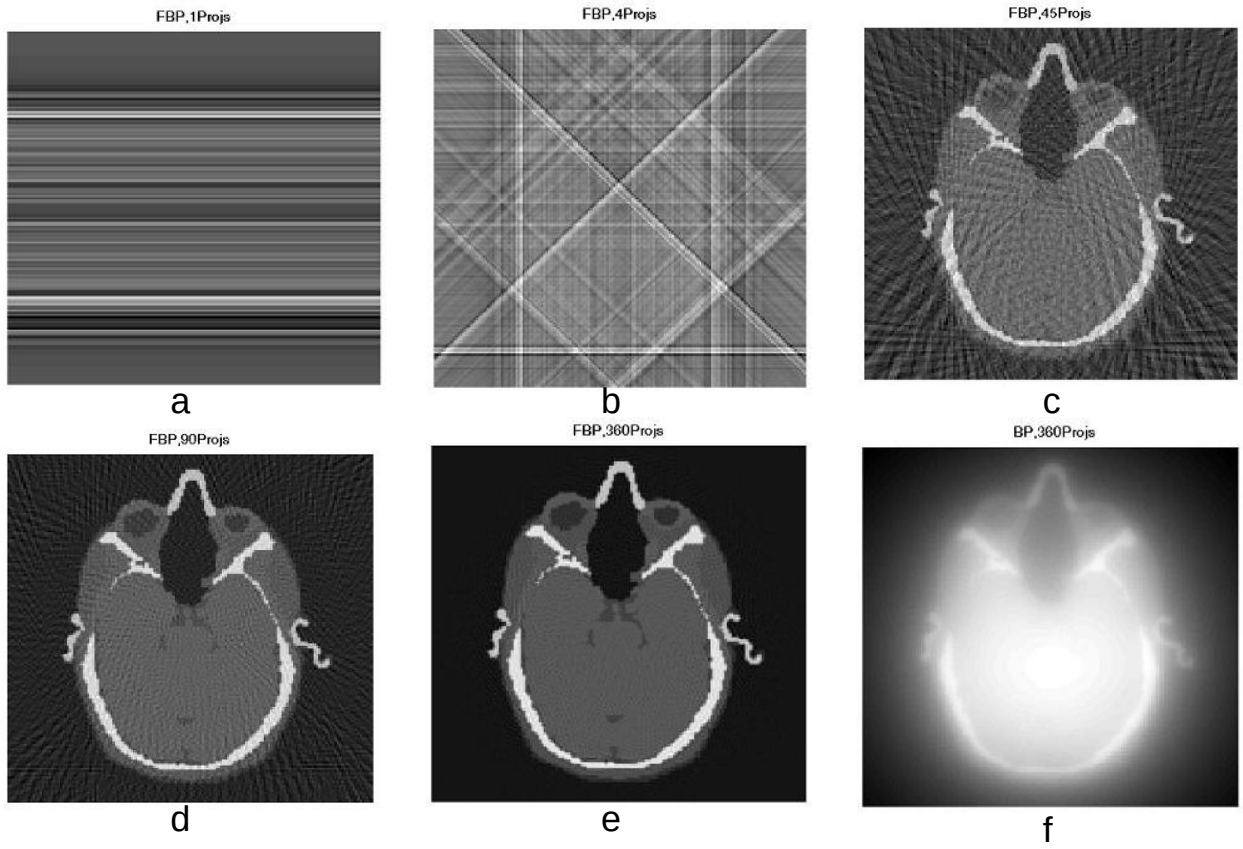

Figure 2.4. FBP reconstruction with different number of projections. (a)-(e) are the FBP reconstruction results of Zubal phantom with 1, 4, 45, 90, 360 projections, respectively. The Ramp-Like filter was applied. (f) is the simple back projection of the same Zubal phantom with the same 360 projections as (e) but without incorporating any filter. In all these reconstructions, the projections were evenly distributed from 0 to 180 degrees in parallel beam geometry.

Fig. 2.5 shows the comparisons between conventional FBP reconstruction and EST reconstruction in different dose levels. From (a) to (c), as the flux was changing from infinity (noise free) to 7.0×10^4 m^{-2}, the streaking artifact and noise on the images become more obvious. Both the resolution and contrast of the image are degraded. For a contrast, for the regularized

EST reconstructions, all the (d) to (f) images, the regularization technique successfully suppressed the noise and made the images clean without artifact and noise, and the contrast and detailed features were still maintained and detectable due to the iterative process.

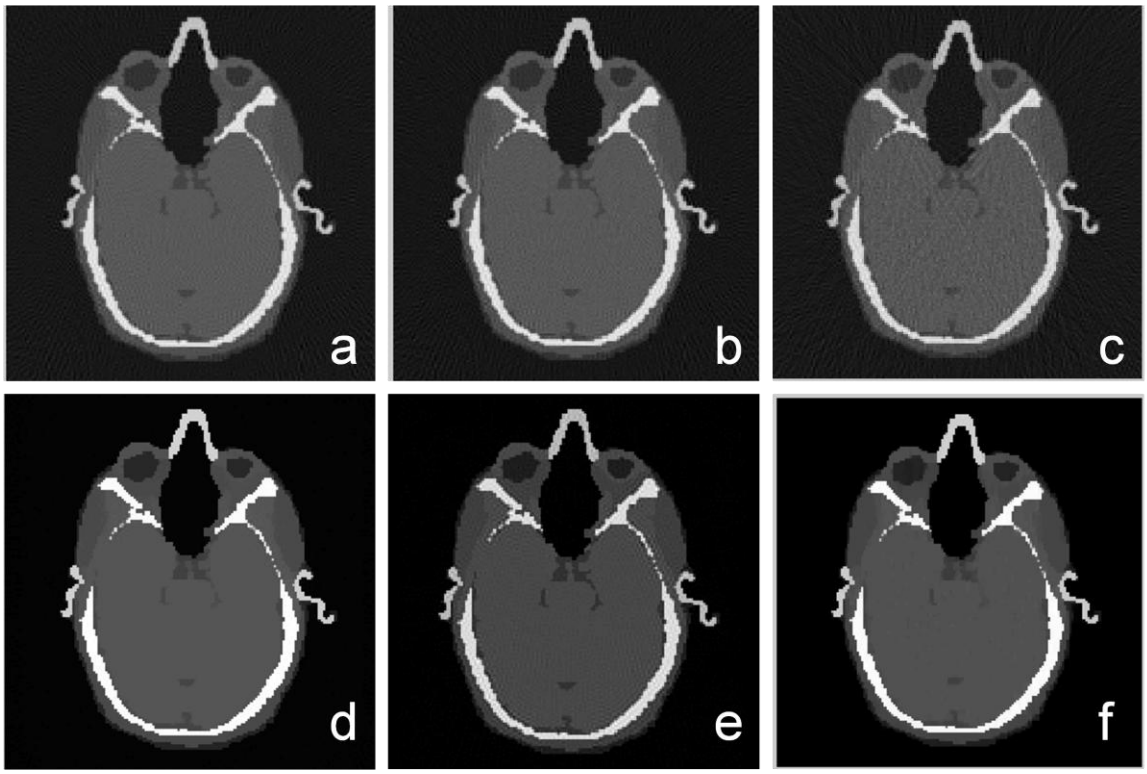

Figure 2.5. Comparison between FBP and EST reconstructions of Zubal phantom under various flux levels. (a) FBP reconstruction of Zubal phantom with no noise added (b) FBP reconstruction of Zubal phantom with flux of 7.0×10^5 m^{-2} (c) FBP reconstruction of Zubal phantom with flux of 7.0×10^4 m^{-2} (d)-(f) are the EST reconstructions of the Zubal phantom with the same noise levels as (a)-(c). For the EST reconstruction, total number of iterations is 20, TV regularization was incorporated.

Fig. 2.6 shows the comparisons between the EST and other iterative reconstruction methods. ART+TV methods obtained comparable good-quality images with a flux of $7.0x10^5$ m^{-2} (low noise), but EST achieved better image quality than ART+TV with a flux of $7.0x10^3$ m^{-2} (high noise). EST and ART+TV clearly outperformed ART due to the lack of noise regularization in the low dose conditions. The reconstructions of EM+TV have better noise performance than ART+TV especially in the extremely low dose situation because the statistical algorithm takes into account the Poisson noise model, which is beneficial for removing the noise in the reconstruction. Therefore, the EM+TV results have similar resolution and noise performance as EST in both dose cases of $7.0x10^5$ m^{-2} and $7.0x10^3$ m^{-2}. But as shown in Table 2 which lists the computation time of FBP, ART, ART+TV, EM+TV and EST with a flux of $7.0x10^3$ m^{-2}, EST requires only one-fifth of the computation time of ART+TV and EM+TV due to the advantage of faster computational speed of Fourier transform over real domain forward and backward projections. And to be noted that, for EST reconstruction, there is an extra step of rebinning and performing Fractional Fourier transform before the iterative process for fan beam geometry, it costs less than 0.5s in this case, which can be neglected compared to the total reconstruction time.

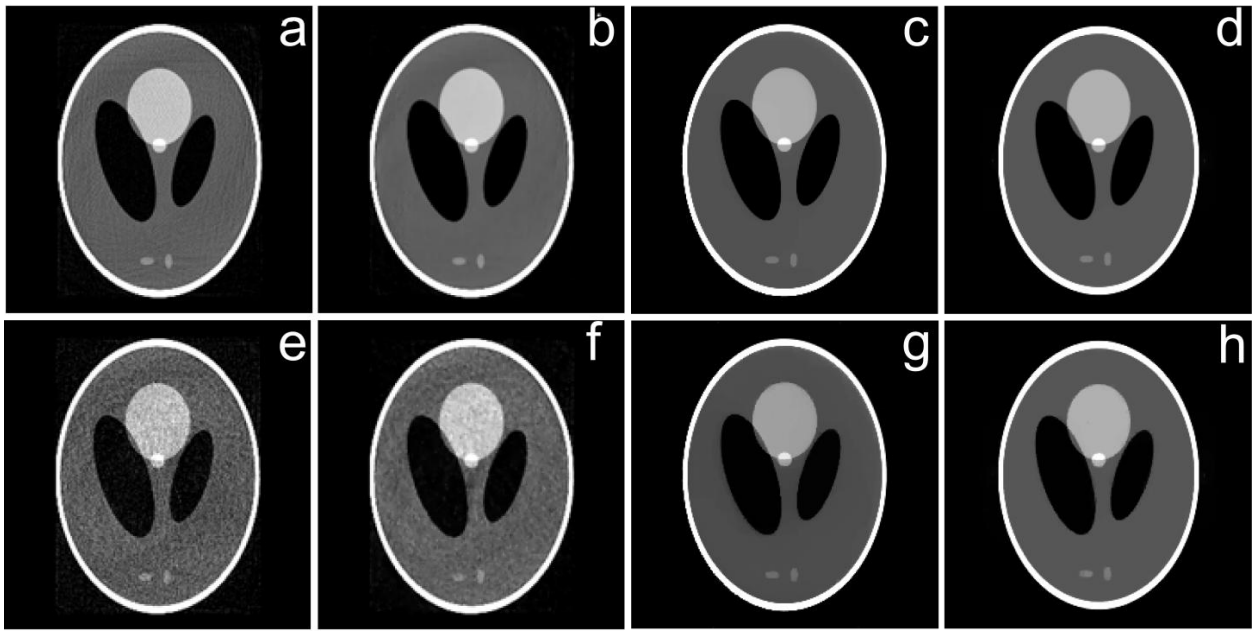

Figure 2.6. Comparisons of Zubal phantom reconstructions using ART, ART+TV, EM+TV and EST under various flux levels. The number of projections is 360 and the number of iteration in each algorithm is 20. (a) ART; flux=7.0×10^5 m^{-2}. (b) ART+TV; flux=7.0×10^5 m^{-2}. (c) EM+TV; flux=7.0×10^5 m^{-2}. (d) EST; flux=7.0×10^5 m^{-2}. (e) ART; flux=7.0×10^3 m^{-2}. (f) ART+TV; flux=7.0×10^3 m^{-2}. (g) EM+TV; flux=7.0×10^3 m^{-2}. (h) EST; flux=7.0×10^3 m^{-2}. EM+TV and EST+TV outperforms ART or ART+TV in the exteam low dose (high noise) conditions.

Methods	Total time (s)	Time per iteration (s)
FBP (‘ifanbeam’ in matlab)		2.0
ART, 20 iterations	259.0	13.0
ART+TV, 20 iterations	272.0	13.6
EM+TV, 20 iterations	286.3	14.3
EST, 20 iterations	53.3	2.7

Table 2.2 Computation time comparison for FBP, ART, ART+TV, EM+TV and EST. Computation time of FBP, ART, ART+TV, EM+TV and EST with a flux of 7.0×10^3 m^{-2} (360 projections number; 512 detectors; 256 x256 pixel reconstruction matrix). The numerical experiment was conducted on Intel® Core™ 2 Duo CPU P8700 with 2.53 GHz and 2.96 GB Memory. The computation time of one iteration EST is comparable with FBP, but EST has much better image quality performance. Compared to ART+TV and EM+TV, EST requires only one fifth of the computational time.

In the numerical experiment for the helical con-beam geometry, we computed the reconstructions of the 3D Shepp-Logan phantom by using FDK, conventional ASSR, and EST with ASSR. Fig. 2.7 shows three different horizontal slices (Z=-30 mm, 0 mm and 23 mm) reconstructed by FDK, ASSR, and EST with ASSR. Visually, ASSR and EST with ASSR produced better image quality reconstructions than FDK. The FDK reconstruction exhibits some artifacts due to the use of a large helical pitch (Fig. 2.7 a-c). Quantitatively, the horizontal and vertical line scans, shown in Figs. 2.7 (j) and (k), indicate that EST with ASSR generated a 3D reconstruction with highest image fidelity and least noise among the three reconstruction methods.

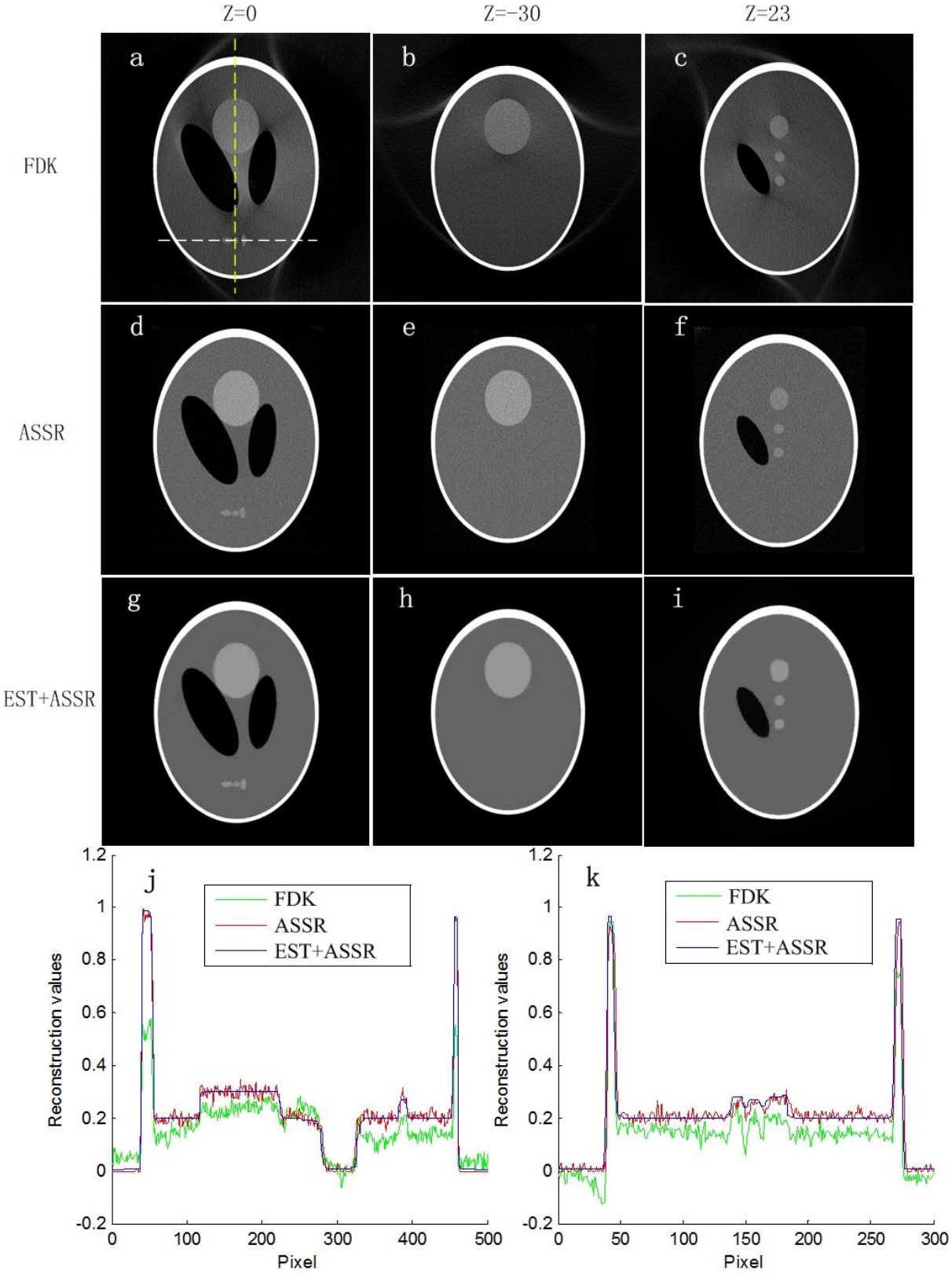
Z=0
Z=-30
Z=23
FDK
ASSR
EST+ASSR
a
b
c
d
e
f
g
h
i
j
k
FDK
ASSR
EST+ASSR
Reconstruction values
Pixel
1.2
1
0.8
0.6
0.4
0.2
0
-0.2
0
100
200
300
400
500
50
150
250

Figure 2.7. Numerical experiment on the reconstruction of helical cone-beam CT data by FDK, conventional ASSR, and EST with ASSR. (a-c) Three representative slices of the FDK reconstruction with Z=-30 mm, 0 mm and 23 mm. (d-f) The same three slices reconstructed by the conventional ASSR method with 2D FBP and TV regularization. (g-i) The same three slices reconstructed by EST with ASSR and TV regularization. (j) Line scan along the yellow line for (a,d,g). (k) Line scan along the white line for (a,d,g).

2.6. Conclusion and discussion

The numerical experiments using Zubal phantom and Shepp-Logan phantom indicate that the regularized EST algorithm outperforms the conventional FBP algorithm in the low dose tomography modalities. This is mainly due to the exactness of PPFFT and inverse PPFFT in EST, the advanced regularization method incorporated and the ability and flexibility of the iterative process that accurately solved the missing values in the Fourier space and guided the reconstructed image to a state, where is a balance between minimized noise and highly consistent with the measurements. We have also implemented and compared EST reconstruction with other regularized iterative reconstruction algorithms such as ART+TV and EM+TV. Though they are all with the iterative structure and denoising techniques, the EST reconstructions still have better low dose performance than ART+TV results when the projections are very noisy. And while the EST method and the EM statistical algorithm produced reconstructions with comparable image quality, EST requires only one fifth of the computation time relative to EM or ART. And finally, the extension of EST to fan-beam and helical cone beam geometry CT data has been

implemented and investigated. Our numerical experiment suggests that the combination of EST with ASSR achieves better reconstructions than FDK and the conventional ASSR method in term of image quality and noise level. Since the main factor that obstructs the utilization of real space iterative algorithm into the real tomography system is the computational speed so far, the computational efficiency and the flexibility to different tomography geometries of the Fourier-based EST algorithm has demonstrated its potential to be implemented into broader tomography applications in the future.

Reference

1. C. Kak, and M. Slaney, *Principles of Computerized Tomographic Imaging*: SIAM, 2001.
2. J. Hsieh, *Computed Tomography: Principles, Design, Artifacts, and Recent Advances*, Bellingham, Washington: SPIE Press Monograph 2003.
3. E. Candes, J. Romberg, T. Tao, "Exact signal reconstruction from highly incomplete frequency information," IEEE Trans. Inf. Theory. **52**, 489–509 (2006).
4. G.H. Chen, J. Tang, and S. Leng, "Prior image constrained compressed sensing (PICCS): a method to accurately reconstruct dynamic CT images from highly undersampled projection data sets," Med. Phys. **35**(2), 660-3, (2008).
5. E.Y. Sidky, and X. Pan, "Image reconstruction in circular cone-beam computed tomography by constrained, total-variation minimization," Phys. Med. Biol. **53**(17), 4777-807, (2008).
6. H. Yu, and G. Wang, "Compressed sensing based interior tomography," Phys. Med. Biol. **54**(9), 2791–2805, (2009).

7. G.H. Chen, et al., “Temporal resolution improvement using PICCS in MDCT cardiac imaging,” Med. Phys. **36**(6), 2130-35 (2009).
8. J.C. Ramirez-Giraldo, et al., “Nonconvex prior image constrained compressed sensing (NCPICCS): Theory and simulations on perfusion CT,” Med. Phys, **38**(4), 2157-67 (2011).
9. L. Ritschl, et al, “Improved total variation-based CT image reconstruction applied to clinical data,” Phys. Med. Biol. **56**(6), 1545-61(2011).
10. L.A. Feldkamp, L.C. Davis, and J.W. Kress, “Practical cone-beam algorithm,” J. Opt. Soc. Am. B: Opt. Phys. 1(6), 612-9, (1984).
11. X. Pan, E.Y. Sidky, M. Vannier, “Why do commercial CT scanners still employ traditional, filtered back-projection for image reconstruction?”, Inverse Problems **25**, 123009 (2009).
12. J. Miao, F. Förster, O. Levi, “Equally sloped tomography with oversampling reconstruction,” Phys. Rev. B. 72, 052103 (2005).
13. J. Miao, et al, “Three-Dimensional GaN-Ga_2O_3 Core Shell Structure Revealed by X-ray Diffraction Microscopy”, Phys. Rev. Lett. **97**, 215503 (2006).
14. E. Lee, et al, “Radiation dose reduction and image enhancement in biological imaging through equally-sloped tomography,” J. Struct. Biol. **164**(2), 221-227, (2008).
15. Y. Mao, B.P. Fahimian, S. Osher and J. Miao, “Development and Optimization of Regularized Tomographic Reconstruction Algorithms Utilizing Equally-Sloped Tomography,” IEEE Trans Image Process. **19**(5), 1259 – 1268, (2010).

16. B.P. Fahimian, Y. Mao, P. Cloetens and J. Miao, “Low dose x-ray phase-contrast and absorption CT using Equally-Sloped Tomography,” Phys. Med. Biol. 55, 5383-5400 (2010).

17. H. Jiang, et al, “Quantitative 3D Imaging of Whole, Unstained Cells by Using X-ray Diffraction Microscopy,” Proc. Natl. Acad. Sci. USA. 107, 11234–11239 (2010).

18. M. C. Scott, C.-C. Chen, M. Mecklenburg, C. Zhu, R. Xu, P. Ercius, U. Dahmen, B. C. Regan, J. Miao, “ Electron tomography at 2.4 Å resolution,” Nature 483, 444-447(2012).

19. Y. Zhao, E. Brun, P. Coan, Z. Huang, A. Sztrókay, P. C. Diemoz, S. Liebhardt, A. Mittone, S. Gasilov, J. Miao, A. Bravin, “High resolution, low dose phase contrast x-ray tomography for 3D diagnosis of human breast cancers”, Proc. Natl. Acad. Sci. USA, under review.

20. S. Matej, J.A. Fessler, I.G. Kazantsev, “Iterative tomographic image reconstruction using Fourier-based forward and back-projectors,” IEEE Trans. Med. Imaging. **23**, 401-412 (2004).

21. Y. Zhang-O'Connor and J.A. Fessler, “Fourier-based forward and back-projectors in iterative fan-beam tomographic image reconstruction,” IEEE Trans. Med. Imag. **25**, 582-9 (2006).

22. W.L. Briggs and V.E. Henson, *The DFT: an owner's manual for the discrete Fourier transform.* 3rd ed. (SIAM, Philadelphia, 1995).

23. R.N. Bracewell and A.C. Riddle, “Inversion of fan-beam scans in radio astronomy,” Astrophysis.J. **150**,427-434,Nov.(1967)

24. G.N. Ramachandran and A.V. Lakshminarayanan , “Three dimensional reconstructions

from radiographs and electron micrographs: Application of convolution instead of Fourier transform," Proc. Nat. Acd.Sci.,**68**, 2236-2240 (1971).

25. K.Lange and R. Carson, "EM reconstruction algorithms for emission and transmission tomography", J. Comput. Assist. Tomog. **8**(2), 302-316 (1984).
26. S. De Francesco and A.M. Ferreira da Silva, "Efficient NUFFT-based direct Fourier algorithm for fan beam CT reconstruction," Proc. SPIE, 5370(666),(2004) .
27. Delaney, A.H. and Y. Bresler, A fast and accurate Fourier algorithm for iterative parallel-beam tomography. IEEE Trans Image Process, **5**(5), 740-53(1996).
28. R.M. Mersereau and A.V. Oppenheim, "Digital reconstruction of multidimensional signals from their projections," Proc. IEEE. **62** 1319–38 (1974).
29. A. Averbuch, et al., "A Framework for Discrete Integral Transformations I—The Pseudopolar Fourier Transform," SIAM Journal on Scientific Computing. **30**(2), 785-803, (2008).
30. D.H. Bailey, and P.N. Swarztrauber, "The fractional Fourier transform and applications," SIAM Review. **33**(3), (1991).
31. J. Miao, P. Charalambous, J. Kirz et al., "Extending the methodology of X-ray crystallography to allow imaging of micrometre-sized non-crystalline specimens," Nature, 400, 342-344(1999).
32. K. S. Raines, S. Salha, R. L. Sandberg *et al.*, "Three-dimensional structure determination from a single view," *Nature,* vol. advance online publication (2009).
33. L.I, Rudin, S. Osher, and E. Fatemi, Nonlinear, " total variation based noise removal algorithms". Physica D, 60, 259-268(1992).

34. T. M. Buzug, *Computed Tomography: from photons statistics to modern cone-beam CT*. (Springer, Berlin, 2008).

35. M. Kachelriess, S. Schaller, W.A. Kalender, "Advanced single-slice rebinning in cone-beam spiral CT," Med. Phys. **27**(4), 754-72, (2000).

36. I.G. Zubal, et al., "Computerized three-dimensional segmented human anatomy". Med Phys, **21**(2), 299-302(1994).

37. A. Averbuch and Y. Shkolnisky, "3D Fourier based discrete Radon transform." Applied and Computational Harmonic Analysis, **15**(1), 33-69 (2003)

38. E. Sidky, C.M. Kao and X.Pan, "Accurate image reconstruction from few-views and limited-angle data in divergent-beam CT", Journal of X-Ray Science and Technology **14**, 119–139(2006).

39. M. Yan and L.Vese, "Expectation maximization and total variation based model for computed tomography reconstruction from undersampled data", Proc. of SPIE, **7961**, 79612X(2011)

40. L.A. Feldkamp, L.C. Davis, and J.W. Kress, "Practical cone-beam algorithm," J. Opt. Soc. Am. B: Opt. Phys. **1**(6), 612-9, (1984).

CHAPTER 3

DOSE REDUCTION RECONSTRUCTION FOR MEDICAL X-RAY CT THROUGH EQUALLY SLOPED TOMOGRAPHY

3.1. Introduction

Since its inception in the 1970s, X-ray computed tomography (CT) has become a revolutionary medical tool in the diagnosis of diseases and visualization of critical interventional procedures (1-4). However, due to the requirement of sufficiently high flux projections from multiple directions for achieving high quality images in tomography, a major concern in medical CT is the unavoidable radiation dose delivered to the patient, especially to the more radiosensitive population such as pediatrics (5-9). According to the 2009 report from the National Council on Radiation Protection & Measurements (10), CT accounts for about 15% of the total radiological examinations, but is disproportionately responsible for approximately 50% of the medical radiation exposure and nearly 25% of the total population exposure. Compared to conventional X-ray chest radiograph, the effective dose of typical medical CT procedures are of one or two orders magnitude higher. Recently many CT device manufacturers and research groups have dedicated to the study to reduce the radiation dose in CT procedures from different approaches, ranging from improving the hardware limitation to developing novice reconstruction algorithm. Among all these works, the combination of real space iterative algorithms with modern

optimization methods has been investigated and proved to be an effective way to reduce radiation dose in CT (11-18).

In this chapter, we incorporated the advanced Non-Local-Means Total Variation regularization into our EST algorithm. We proposed a Fourier based iterative reconstruction algorithm which is adapted for fan beam medical CT scanner. We implemented the algorithm on Siemens SOMATOM Sensation 64 scanner at UCLA 100 Medical Plaza and performed a series experiments with image quality phantoms and clinical pediatric patient data sets. For the contrast and resolution image phantoms, we performed the experiments and measured the projections while systematically lowering the radiation dose by reducing the photon flux, then carefully evaluated the image quality of the results from both EST algorithm and conventional FBP algorithm. The comparison evaluations are both quantitative and qualitative. For the pediatric patient data set, we simulated a series low dose conditions by adding Poisson noise to the measured projections then performed reconstructions by both EST and FBP. The results are also compared and evaluated.

3.2. Methods

3.2.1. Data preparation

All the experiment data sets were acquired from the Siemens SOMOTOM Sensation 64 CT scanner (Siemens Medical Solutions, Forchheim, Germany) at UCLA 100 Medical Plaza. The

array detector of the scanner consists of 40 rows in the longitudinal (z) direction; the central 32 rows are of 0.6mm slice width while the outer 8 rows have a width of 1.2mm each. In each row, there are 672 physical detector channels (19, 20). We utilized the collimation set up of 32*0.6 mm and choose the projections acquired from the center slice (slice 16) for our fan beam reconstructions. The fig.1a shows the geometry of the scanner at the central slice: the red dot represents the source while the blue dot represents the rotation center. The distance from the source to the isocenter is R_F = 570mm, the distance from the source to detector is R_{FD} = 1040mm and fan angle equals to Φ = 52 º.

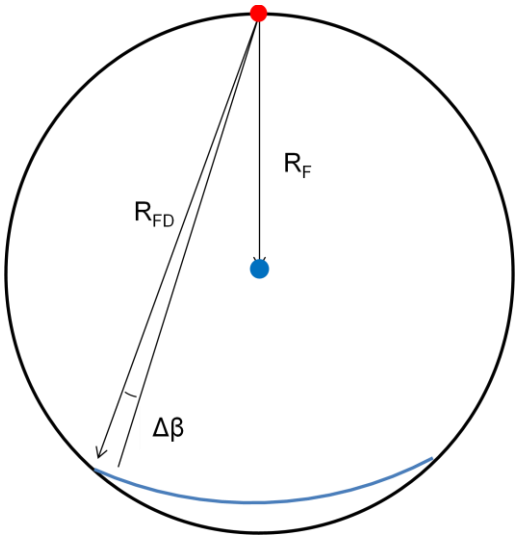

Figure 3.1. Geometry of the central slice of Siemens SOMATOM Sensation 64 CT scanner. Red dot represents the source, blue dot represents the isocenter. R_F = 570mm is the distance from source to isocenter; R_{FD} = 1040mm is the distance from source to detector. The fan angle Φ = 52 º. $\Delta\beta = 180^0/2320$ is the physical detector angular increment.

Before inputting the measured projections into the reconstructions, there are two data preparation steps are necessary for the EST reconstruction algorithm. First, this specific medical scanner we studied utilized a technique termed Flying Focal Spot (FFS) to doubling the sampling density to reduce the aliasing artifact while increase the projection resolution by 2. So in the transaxial direction, there are actually 1344 data channels when the α-FFS is using with the size of each channel is ½ of the physical channel size. In the z direction, there will be actually 64 slices when the z-FFS is turned on. z-FFS was optional turned off during our experiment while α-FFS was enforced on. Therefore, an interlace step is required before any reconstruction. Fig. 3.2 (a) shows the α-FFS geometry. The variation in R_F due to $\partial\ \alpha$ is negligible and $\partial\ \alpha$ is given by Eq. 3.1(19).

$$\partial\alpha = \frac{1}{4}\,\Delta\beta\,\frac{R_{FD}}{R_D} \qquad (Eq.3.1)$$

The raw data structure read by MATLAB is shown as Fig. 3.2 (b). When the source moved from the initial gantry position θ_1, because of the α-FFS, the source will wobbling at two nearby positions then row1 and row2 were recorded. Then the source moved to the next gantry position θ_2, row3 and row4 were recorded. There are 672 channels for each row. A interlace between row1 and row2, row3 and row4, row5 and row6… were performed. Since the scans we performed were all in full axial mode, there are total 1160 gantry positions for each scan and the after interlaced fan beam sinogram size is 1160 in rows and 1344 in channels. Fig. 3.3 (b) shows an example of the fan beam sinogram after the interlaced procedure.

The beneficial of Fourier based reconstruction algorithm such as EST is that, through the central

slice theorem and the existence of PPFFT and adjoint PPFFT, the calculation of forward and backward projection can be achieved in more efficient and accurate compared to image based reconstruction algorithms. However, according to the formation of central slice theorem stated in Chapter1, to achieve the data on one line at a specific angle in Fourier slice, 1D Fourier transform needs to be performed on the 1D parallel projection values along the same angle. As a result, to directly utilize the information in Fourier space, the projection data must be in the parallel beam geometry (21). To increase the efficiency of data acquisition, most medical CT scanners nowadays are in the cone beam geometry, which means the central slice of the projections are in fan-beam geometry. Furthermore, to take full advantage of the EST algorithm, the input projections should be along the equally-sloped lines in the pseudo-polar grid instead along the equally angle increment lines in the polar grid. Because of these two reasons, prior to initiating the EST iterative algorithm, the second step in the data preparation is to transform the fan beam projections to equally-sloped lines in a pseudo-polar grid. We utilized the common rebinning method, implemented with two 1D interpolations (4). The relation of the coordinates between a ray in the fan beam geometry $p(\theta,\psi)$ and a ray in the parallel geometry $p(\phi,\xi)$ is defined as:

$$\begin{cases} \phi = \theta + \psi \\ \psi = \arcsin\left(\frac{\xi}{D}\right) \end{cases} \qquad (Eq.2.12)$$

where θ is the projection angle in the fan beam geometry, ψ the fan angle of the ray, ϕ the projection angle in the parallel beam geometry, ξ the perpendicular distance from the origin, and

D the distance from source to rotation center. Fig. 3.3 (a) shows this parallel beam geometry and the fan beam geometry. The main change we made to the common rebinning method is that ϕ is at equally-sloped angular intervals. Note that, although the rebinning step requires interpolations, our numerical simulations indicate that this process does not introduce much additional noise or artifacts as long as the fan-beam projections are finely sampled. It is also important to point out that the rebinning process needs to be applied only once, prior to the initiation of the iterative process, after which point, the Fourier transform of the rebinned projections are utilized as measurement constraints. Additionally, the parallel projections are not calculated at all the 2N lines of the pseudo-polar grid, rather only limited portion of the pseudo-polar grid in Fourier space are filled with these rebinned measurement data, and the rest of the lines are filled in by the iterative algorithm as the reconstruction is solved for.

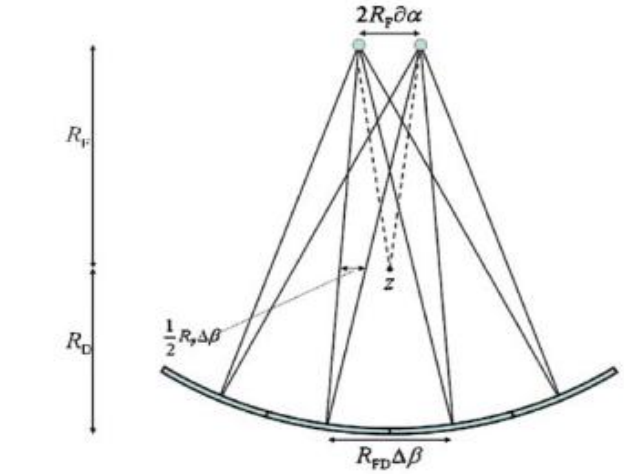

(a)

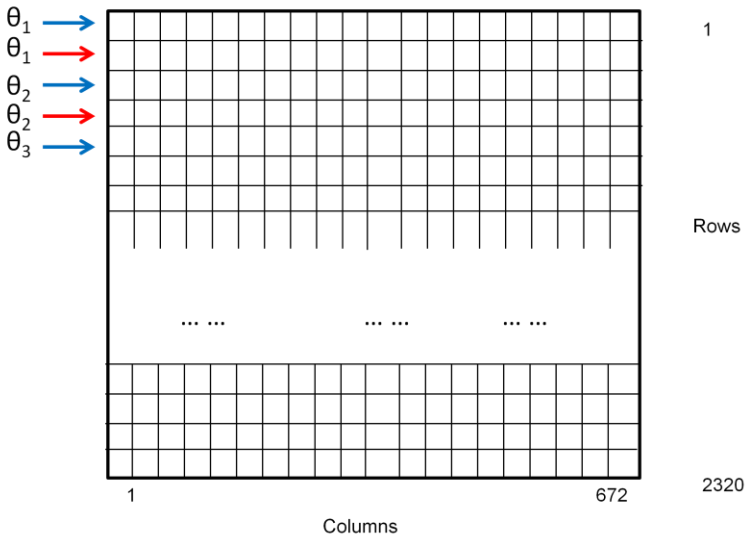

(b)

Figure 3.2. The geometry and data structure from the α-Flying Focal Spot (α-FFS) technique. The technique is implemented in Siemens SOMATOM Sensation 64 slice CT scanner. (a) the focal spot is wobbling at two positions for each acquisition angle in the transaxial plane. (b) Raw readout data structure. The two rows indicated by the blue and red arrows from the same θ store the projections recorded from two focal spot positions at the same acquisition angle.

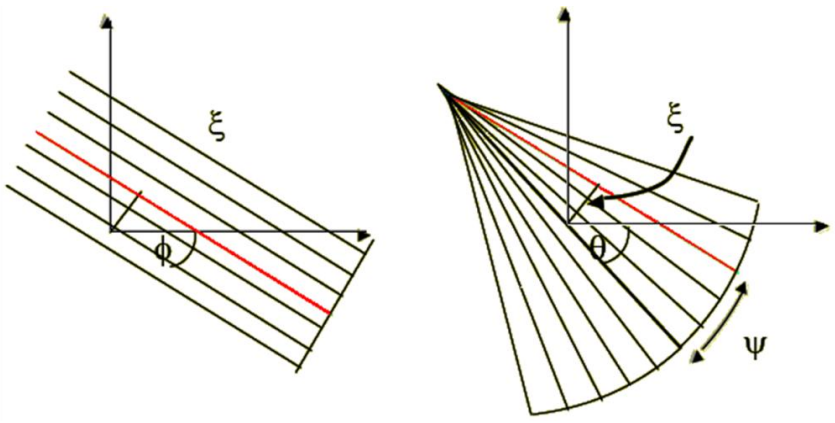
ξ
ϕ
ξ
θ
ψ

(a)

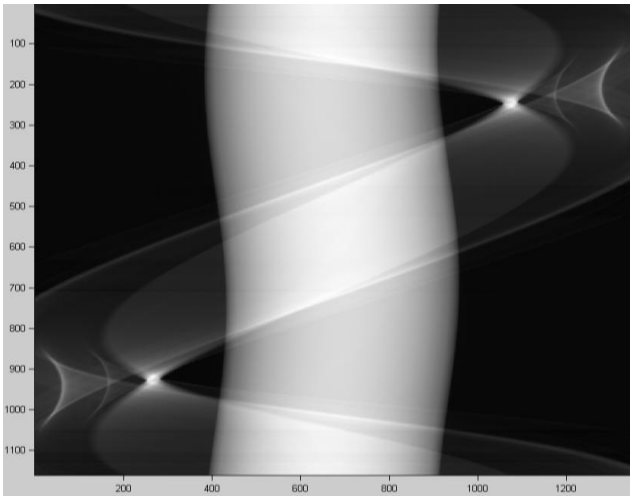
100
200
300
400
500
600
700
800
900
1000
1100
200
400
600
800
1000
1200

(b)

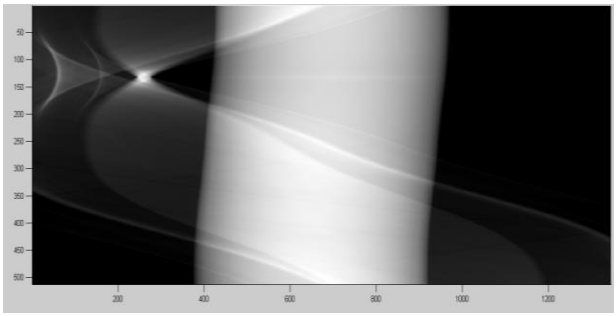

(c)

Figure 3.3. Fan beam to parallel beam rebinning. (a) Parallel-beam geometry (left) and the Fan-beam geometry (right). (b) and (c) are the sinogram of the central slice of one scan of EMMA phantom with 400mAs flux setting. (b) The fan-beam sinogram after detector interlaced. It is 1344 in detector channels and 1160 in projection angles. (c) The parallel beam geometry sinogram of (b) after rebinning procedure. It is 1344 in detector channels and 512 in projection angles. The angels are followed the EST acquisition angle rules.

3.2.2. Non-Local Total Variation Based Equally Sloped Tomography

In the conventional 2D tomography reconstructions, the series of projections are acquired around the isocenter with constant angular increment. This equally-angled acquisition type, after performing 1D Fourier transform along these projections, will result in a polar distribution of measured data, while the reconstructed images have to be in the Cartesian grid. And since it is believed that there is no direct exact FFT algorithm can be constructed between the polar and Cartesian grids (22-24), one directly way is to do interpolation in the Fourier space from the polar grid distribution points to Cartesian grids. However, unlike the interpolation in object domain which is constrained in local region, each point in Fourier space corresponds to all the points in the image domain, which means that, the interpolation in Fourier space could introduce error and degradation all over the whole reconstructed image. Recently, it has been shown the existence of an algebraically exact FFT algorithm between the pseudo-polar and Cartesian grids denoted the PPFFT (25, 26). Fig. 3.4 shows the pseudo-polar grid and PPFFT. As depicted in the

Fig. 3.4, for a $N \times N$ Cartesian grid, the pseudo-polar grid is defined by a set of 2N lines, each line consisting of 2N grid points mapped out on N concentric squares. The $2N$ lines are subdivided into two groups: a horizontal group (in gray) defined by y = s*x and a vertical group (in red) defined by x = s*y, in both equations s represents the slope and $|s| \leq 1$. These pseudo-polar lines are termed "equally-sloped" since the successive lines in both groups change by an equal sloped increment as opposed to a fixed equal angled increment as in the polar grid. Unlike the polar grid, the distance between sampling points on the individual lines of the pseudo-polar grid varies from line to line as indicated in Fig. 3.4. So instead of using the conventional 1D Fast Fourier transform (FFT), the fractional Fourier transform (FrFT) can be used here to vary the output sampling distance of the Fourier transform (28). The 1D FrFT is defined by

$$F_\alpha(k) = \sum_{X=0}^{N-1} f(x)\exp\left(-\frac{i2\pi\alpha kx}{N}\right) \qquad \alpha = \begin{cases} \frac{1}{\cos(\theta)} & Horizontal\ Set \\ \frac{1}{\sin(\theta)} & Vertical\ Set \end{cases} \qquad (Eq.3.3)$$

In this equation, $F_\alpha(k)$ is the 1D FrFFT, $f(x)$ is the 1D tomographic projection, k and x are the coordinates in Fourier and object space, and α is the parameter that determines the distance between the sampling points in each of the 2N lines. The pseudo-polar grid and the PPFFT algorithm were originally developed to interpolate tomographic projections from the polar to the Cartesian grid in reciprocal space (25, 26). The idea of acquiring tilt-series at equal slope increments and then combining the PPFFT with iterative algorithms for tomographic reconstructions was first proposed by Miao *et al*. in 2005 (29).

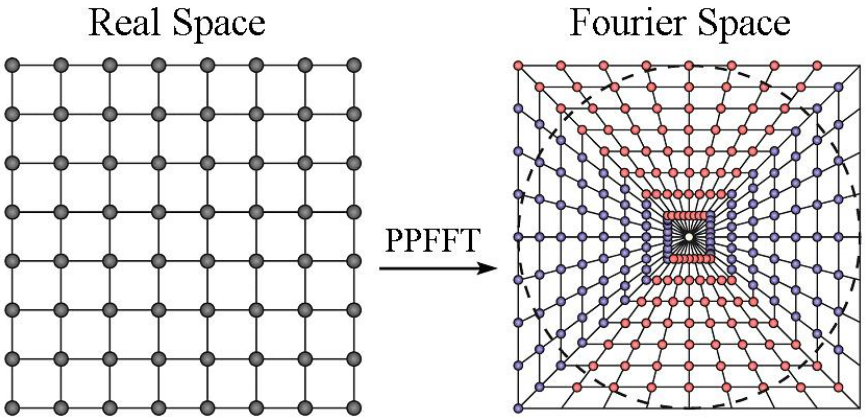

Figure 3.4. Geometrical representation of a Cartesian and a pseudo-polar grid. The grids are related by the algebraically exact PPFFT. The dotted circle represents the resolution circle.

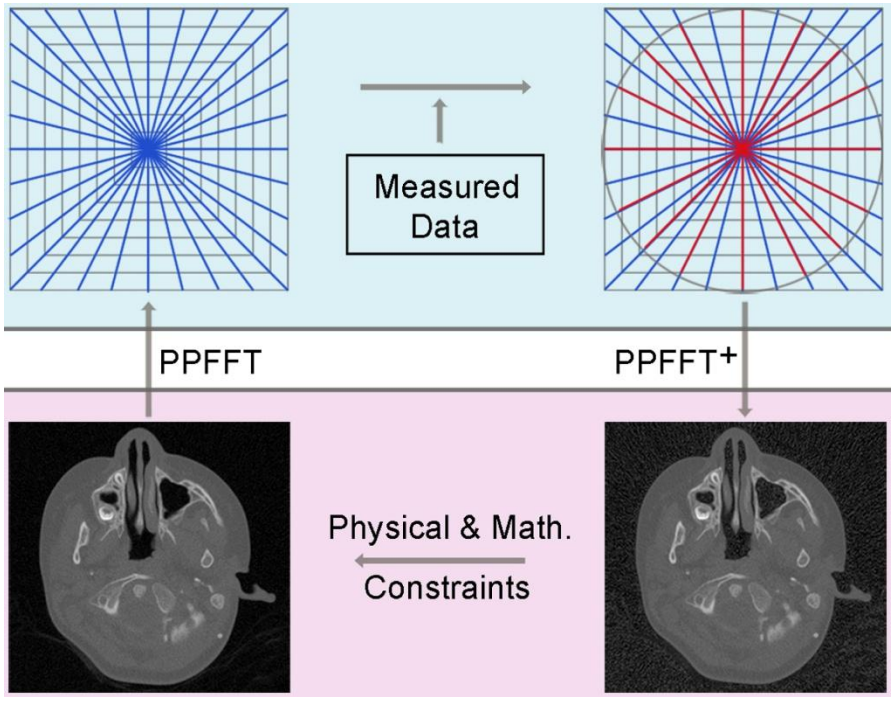

Figure 3.5. Schematic of the EST method that iterates back and forth between real and Fourier space. The forward transform from a Cartesian grid in real space (bottom-left) to a pseudo-polar grid in Fourier space (top-left) is performed by the PPFFT. The backward step from Fourier space to real space is performed by the adjoint transform of the PPFFT ($PPFFT^{+}$). In each iteration, physical and mathematical constraints are enforced in real space (bottom-right), while measured data (red lines in top-right) is applied in Fourier space. An error metric is used to monitor the convergence of the iterative algorithm.

Although the PPFFT and its inverse provide an algebraically exact way to do the FFT between the Cartesian and pseudo-polar grids, three difficulties limit its direct application to tomographic reconstructions. First, to accurately invert the Fourier data using the PPFFT, knowledge of 2N data points along the 2N equally-sloped lines is needed (26). This requires a large number of projections and is not desirable in experiment due to radiation dose or technical restrictions. Secondly, the pseudo-polar grid points past the resolution circle (indicated by the dotted circle in Fig. 3.4) cannot be experimentally obtained (27) and thus exact reconstructions through the inverse PPFFT are not possible. Third, the clinical measurements are always with noise due to the restriction or concern of the radiation dose delivered to patient. Less flux is always designated but it will degrade the projections quality by having higher noise level. In order to enhance the image quality and reduce radiation dose at the same time, physical constraints and mathematical regularization have to be applied in the image reconstruction. To overcome these difficulties, the EST method for medical CT was developed, which iterates back and forth between real and Fourier space (28-35) and structured to reach the compromise between both

spaces, applying physical and mathematical constraints in object space and enforcing experiment projections in Fourier space. The algorithm starts with padding each projection with same number of zeros on both sides and calculating its oversampled Fourier slice in the pseudo-polar grid (red lines in Fig. 3.5 top-right) through 1D FrFT, which will not introduce any interpolation in Fourier space as the conventional FFT does. The oversampling concept (*i.e.* sampling the Fourier slice at a frequency finer than the Nyquist interval) has been widely used to solve the phase problem in coherent diffraction imaging (36-38). In the EST method, we achieve oversampling by surrounding the object in real space by mathematical zeros, a region we called 'support' and utilized them as constraint in object space. These zeros does not provide any extra information about the object, but they provide additional constraints in real space and extract more correlated information among different projections in Fourier space during the iterative process. Following the interlacing and rebinning process described before, in the first iteration, the grid points outside the resolution circle and on the missing projections (blue lines in Fig. 3.5 top-right) are set to zero. The algorithm then iterates back and forth between real and Fourier space using the PPFFT. As shown in Fig. 3.5, the j^{th} iteration consists of the following 6 steps:

i) Apply the adjoint transform to the Fourier-space slices $F_j(\vec{k})$, and obtain a real-space image, $f_j(\vec{r})$ (Fig. 3.1 (b) bottom-right). Here the adjoint PPFFT instead of the inverse PPFFT is used. Because the former is implemented through a conjugate gradient method and can be computed much faster than the latter without compromising the accuracy (31).

ii) Derive a new object, $f_j^r(\vec{r})$, by applying mathematical regularizations to $f_j(\vec{r})$ (41,41). In our reconstructions, we applied the non-local total variation regularization

(NLTV) (41) once in every other iteration. The nonlocal total variation regularization is defined as:

$$J_W(f) = \int \sqrt{\int \left[f(p_1) - f(p_2)\right]^2 w_h(p_1, p_2) dp_1 dp_2} \quad \text{(Eq. 3.4)}$$

Where the weight function $w_h(p_1, p_2)$ describing the similarity between the patches around different pixels p_1 and p_2 and h is the parameter to define the similarity between patches .The object is regularized by minimizing:

$$\min_f J_w(f) + \frac{\lambda}{2}\left\| f - f_j \right\|^2 \quad \text{(Eq. 3.5)}$$

λ is the parameter that controls the strength of TV-regularization. The smaller the λ, the stronger the regularization is. Compared to the local TV, NLTV presents a new way to do image regularization. The local TV performs local smoothing and can preserve the edge well. But sometimes it will over-boost or over-smooth the texture and eliminating the small scale features. It works best for piece-wise constant type of images. The clinical CT images are much more complicated and have much more important small features compared to piece-wise constant phantom images, which means simply apply TV on the image would likely to produce artifact patches while suppressing noise. On the other hand, the NL-TV searches the similar patches around the defined window and performs a weighting TV minimization based on the

similarity. It has the assumption that the natural images contain repeated structures instead of repeating pixels. The method has been proved to be able to adopt the advantage of edge preserving in local TV but the nonlocal weighted graph it uses present the similarity of different pixels instead of direct subtraction, which can preserve fine structures and textures better.

iii) A support S is determined based on the zero padding of the projections to achieve oversampling. Outside the support $f_j^r(\vec{r})$ is set to zero and inside the support, the negative values of $f_j^r(\vec{r})$ are set to zero as a physical constraint (Eq. 3.6). A new image is obtained, defined as $f_j^{'}(\vec{r})$ (Fig. 3.5 bottom-left).

$$f_j^{'}(\vec{r}) = \begin{cases} f_j^r(\vec{r}) & \text{if } \vec{r}\,! \in \text{S or } f_j^r(\vec{r}) > 0 \\ 0 & \text{if } \vec{r} \in \text{S or } f_j^r(\vec{r}) < 0 \end{cases} \qquad (Eq.\,3.6)$$

iv) Apply the PPFFT to $f_j^{'}(\vec{r})$ and obtain updated Fourier-space slices, $F_j^{'}(\vec{k})$ (Fig. 3.5 top-left);

v) Obtain the Fourier slices for the (j+1)th iteration, (Fig. 3.5 top-right), by replacing $F_j^{'}(\vec{k})$ with the measured Fourier slices (red lines in Fig. 3.5). The grid points outside the resolution circle and on the missing Fourier slices remained unchanged.

vi) An error metric is calculated,

$$Error = \frac{\sum_k \left| F_j^{'}(\vec{k}) - F(\vec{k}) \right|_{k \le R}}{\sum_k \left| F_j^{'}(\vec{k}) + F(\vec{k}) \right|_{k \le R}} \qquad \text{(Eq. 3.7)}$$

where $F(\vec{k})$ represents the measured Fourier slices, $F_j^{'}(\vec{k})$ is the calculated Fourier slices in the jth iteration, and *R* is the radius of the resolution circle.

In general, the algorithm is stopped when the error does not decrease by more than 1% from the previous iteration. In actual experiments, it is automatically terminated when the error becomes stabilized after about 20 iterations. In order to have the reconstruction consistent with the measurement and will not be over smoothing, the object space regularization step was turned off for the last iteration.

3.3. Experiment Design

The EST method has been validated thoroughly for the parallel beam geometry in our former research work (28-35). In this work, the data sets were acquired from a Siemens SOMATOM Sensation 64 scanner with axial mode on and only the central slice was selected to validate the feasibility of the EST method for the fan beam geometry for the first time in this paper. A total of 1160 projections were acquired from 0°-360° with equally angle increment. After data interlacing and correcting due to the α-FFS, there were 1344 detector channels and the reconstruction matrix size was 1344x1344 pixels. A rebinning step was performed prior to initiating the algorithm in order to transform the fan beam projections to parallel projections along equally-sloped lines of the pseudo-polar gird as described before.

3.3.1. Phantom Studies

The Siemens image quality phantom (EMMA) (42) was used to quantify the amount of CT dose reduction achievable by the EST method. The phantom contains resolution inserts to measure the image resolution, and contrast inserts to measure the image contrast (42). The three inserts are shown in Fig. 3.6. The diameter of the contrast inserts in Fig. 3.6 (a) & (b) are 3 mm, 5 mm, 7 mm, 10 mm, 20 mm, with varying normalized electron density ratios, relative to solid water background, 1.01 (1% signal), 1.03 (3% signal), 1.05 (brain), 1.07 (liver), 1.09 (inner bone), 1.17 (acrylic), 1,48 (bone), and 0.001(air), respectively for the regions labeled with number 1 to 8. The information for the resolution insert is shown in Table. 1, the resolution bars, which consist of air, start at a resolution of 0.067 line pairs per mm in group 1, to a resolution of 1 line per mm in group 11. The EMMA phantom was systematically scanned at different flux settings, ranging from a maximum of 583 mAs to a minimum of 39 mAs. All scans are performed under axial mode with the tube current modulation off, z-FFS off, α-FFS was turned on and the voltage set to 120kVp. The FBP reconstructions are performed with a standard uncropped ramp filter in conjunction with cubic interpolation for the back projection process for all doses. In the case of 39 mAs dose, the FBP reconstruction result is at last denoised by nonlocal total variation regularization (i.e. FBP+NLTV). The 39 mAs EST reconstruction was computed by using the iterative algorithm described in II.B. Both FBP+NLTV and EST used the same regularization parameter (0.0035).

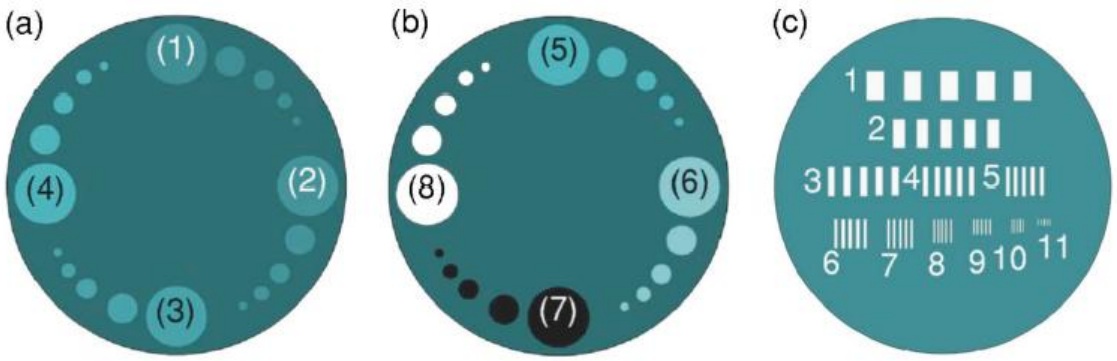

Figure 3.6. The three inserts from Siemens' image quality EMMA phantom. (a) Low contrast insert. (b) High contrast insert. (c) Resolution insert.

Bar group	Width (mm)	Height (mm)	Line pair per mm
1	7.5	12.0	0.067
2	5.0	12.0	0.1
3	3.3	12.0	0.15
4	2.5	12.0	0.2
5	2.0	12.0	0.25
6	1.67	12.0	0.3
7	1.25	12.0	0.4
8	1.0	10.0	0.5
9	0.83	6.6	0.6
10	0.62	5.0	0.8
11	0.50	4.5	1.0

Table 3.1. Information for the resolution insert for EMMA phantom. The width, height and resolution value for the bar groups in the resolution insert from Siemens' image quality phantom, EMMA are shown in the table.

3.3.2. Patient Studies

To further quantify the radiation dose reduction in clinical environment with the EST method, a pediatric patient data set consisting of a cranial scan of an anonymous 8 year old boy was used. The scan was originally acquired under axial mode with a voltage of 120kVp and a flux setting of 140mAs. There are 6 contiguous axial scans total, the central slices of which were used for study and reconstruction. However, unlike the phantom studies, it is not possible to acquire repeated scans of the patient at different flux settings due to radiation dose concerns. To address this issue, an algorithm to simulate low dose patient data based on existing scans (43, 44) was implemented. Using this algorithm and the pediatric patient data set with a flux setting of 140 mAs, we generated CT scans at 39 mAs, the lowest possible flux setting of the Siemens Sensation SOMATOM 64 scanner. In addition, the setting of 14 mAs, which is one of tenth of the original data set, is simulating. Both the FBP and EST reconstructions are computed in the same manner as the phantom studies.

3.3.3. Evaluation methods

We firstly evaluate overall image quality of the reconstruction results by observing the visibility of the fine and low contrast structures relative to the reconstruction of such objects acquired under high dose acquisition protocols that provide the benchmark image. The correlation between the reconstructed image and the benchmark image can then be quantified by using cross-correlation. In the phantom studies, the contrast and resolution inserts are used to evaluate

the image contrast and image resolution at different flux levels. In phantom studies, quantitative comparisons are done by measuring the mean values and their standard deviation at various contrast regions to calculate the SNRs and the CNRs as Eq. 3.8. I_{ROI} represents the pixel values in regions of interest.

$$SNR = \frac{Mean(I_{ROI})}{Std(I_{ROI})}$$
$$CNR = \frac{2 \times \left| Mean(I_{ROI_1}) - Mean(I_{ROI_2}) \right|}{Std(I_{ROI_1}) + Std(I_{ROI_2})} \qquad \text{(Eq. 3.8)}$$

The resolution performance is evaluated by comparing the reconstruction results from the resolution insert in different flux setting. The line profiles along the high resolution bars are plotted and compared. The reconstruction results of pediatric data sets are also compared by different flux and reconstruction method. SNRs and CNRs are measured for the regions of interests.

3.4. Results

3.4.1. Contrast Phantom

The detectability of low contrast features is one of the important criteria in low dose reconstructions, especially when using an iterative algorithm that incorporates regularization

methods. The regularization methods, which are usually controlled by one or more parameters, could possibly erase the small low contrast features when they are not implemented or chosen in a proper way. So we have quantified the image contrast and quality of the EST and FBP reconstructions at different flux settings by using the medium and low contrast inserts of the EMMA phantom. Figs. 3.7 (a-e) show the FBP reconstructions at 583 mAs, 140 mAs, 39 mAs, FBP+NLTV reconstruction at 39 mAS and EST reconstruction at 39 mAs of the medium contrast insert, respectively. This inserts consist of 4 different sets of the cylinders, and the zoomed views of the lowest contrast set (9% signal) of the cylinders are shown in Fig. 3.2 (f-j). The SNRs and the CNRs were also calculated for the largest diameter cylinder (indicated in Figs. 3.7 (f-j)). Compared to the FBP and FBP+NLTV reconstructions at 140mAs and 39mAs, the EST reconstruction at 39mAs (Figs. 3.7 (e) and (j)) exhibits better image quality and are almost consistent with the reference reconstruction (FBP at 583mAs). As indicated by the arrows in the zoomed views (Fig. 3.7 (f-j)), the smallest cylinder (3mm in diameter) in the 39mAs EST reconstruction is as visible as that in the 583 mAs FBP reconstruction, but it almost disappears in 140 mAs FBP, 39 mAs FBP and FBP+NLTV reconstructions. Also, the SNRs and CNRs of the 39mAs EST reconstruction outperform all FBP, FBP+NLTV ones, including the 583 mAs reference reconstruction. However, the SNRs and CNRs have kind of limitations and depend on the place chosen. Also, NLTV denoising could help to improve SNRs and CNRs but potentially results in patchiness phenomenon in the case of heavy noise.

Fig. 3.8 shows the reconstruction images for the low contrast inserts of EMMA phantom. Low dose resulted in serious noises which influence the image quality of the reconstructions of low

contrast inserts. It should be noticed that the lowest contrast set (0.1% signal higher than background) is not clear visible for all the reconstructions. For the highest contrast set (7% signal), all the five cylinders can be identified clearly in all the reconstructions except for the FBP+NLTV. This shows that the regularization method could erase some small low contrast details and these details cannot be recovered because the onetime back projection algorithm such as FBP is lack of the feedback system. On the other hand, the EST can retrieve these lost details though the iterative process. The Figs. 3.8 (f-j) show the zoomed view of the second highest contrast set (5% signal) of the cylinders. The second smallest cylinder (5mm in diameter) indicated by arrows completely disappears in the 39 mAs FBP and FBP+NLTV reconstructions and is almost invisible in the 140 mAs FBP reconstruction, while it is still visible in the 39 mAs EST reconstruction.

For both medium and low contrast inserts, the SNRs and CNRs of the 20 mm cylinder regions circled by dashed lines in Fig. 3.7 and Fig. 3.8 are calculated. The CNRs were calculated relative to the uniform center region. The calculated results for the 9% signal and 5% signal contrast sets are shown in the zoomed views in Fig. 3.7 and Fig. 3.8. It is noted that the SNR and CNR for the 39mAs EST reconstruction is higher than all the other reconstructions, including 583mAs FBP, 140mAs FBP, 39mAs FBP and 39mAs FBP+NLTV. However, we cannot say that 39mAs EST+NLTV has better performance than 583mAs FBP since the regularization method always minimize the noise and boost the calculated values of SNR and CNR. But compared to 140mAs FBP, 39mAs FBP, visually the 39mAs EST images are much cleaner with less grainy noise, and the contrast sets can be detected better from the background. And the 39mAs FBP+NLTV

images, though are also quite clean and high in SNR and CNR values due to the regularization algorithm, lost small low contrast features and are degraded by the artifact patches. It is the evidence of the fact that the advanced iterative process in EST provides a feedback loop that corrects the artifact caused by regularization while minimize the noise on the images.

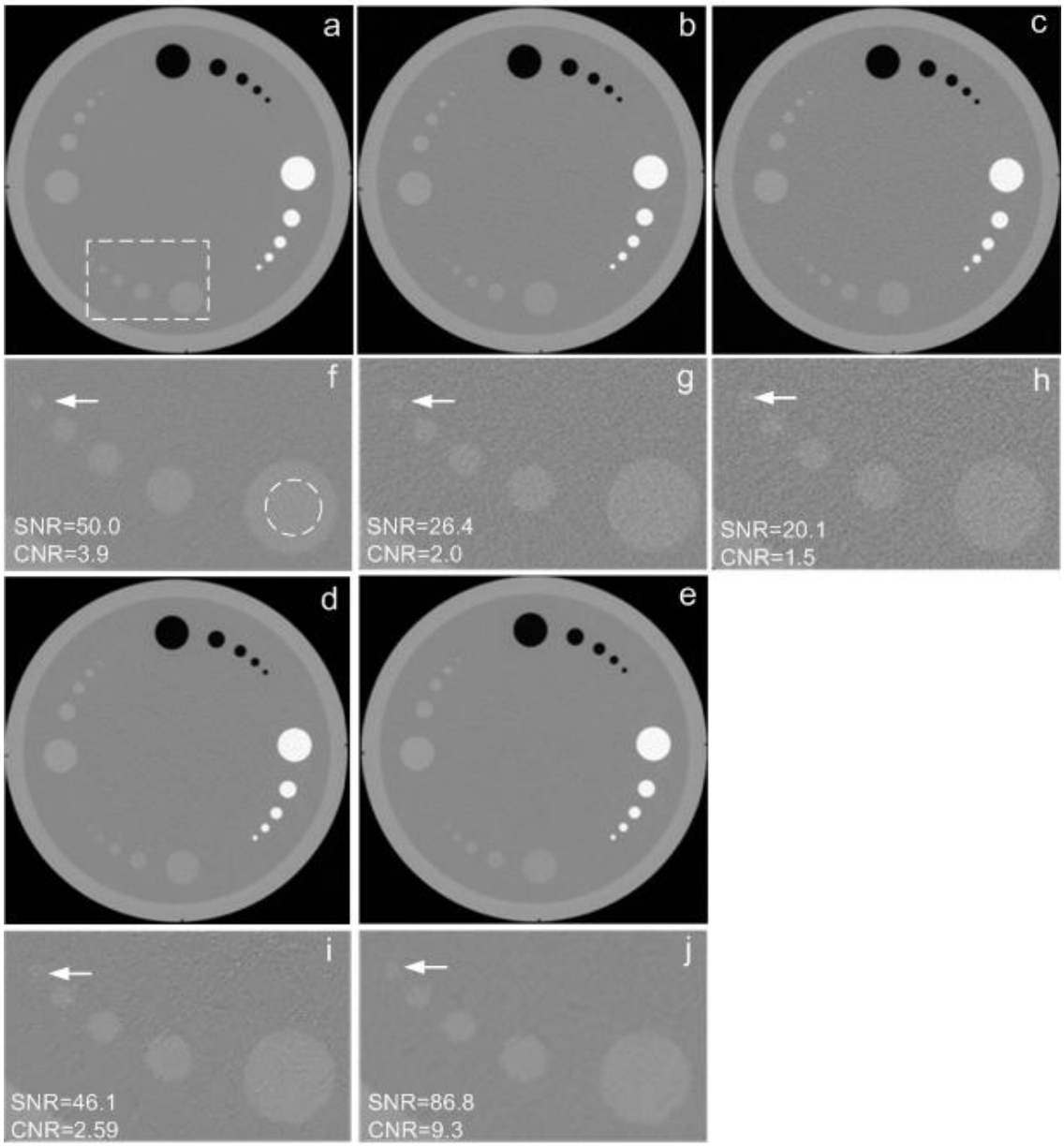

Figure 3.7. Comparative reconstructions of the medium contrast insert of the EMMA phantom. Grayscale window: [-1000,1000] HU. Reconstructions of (a) 583 mAs FBP, (b) 140 mAs FBP, (c) 39 mAs FBP, (d) 39 mAs FBP+NLTV and (e) 39 mAs EST. (g)-(j) Zoomed images of the rectangular region from (a)-(e), where the SNRs and CNRs were calculated for the largest diameter cylinder, indicated by the circle in (f).

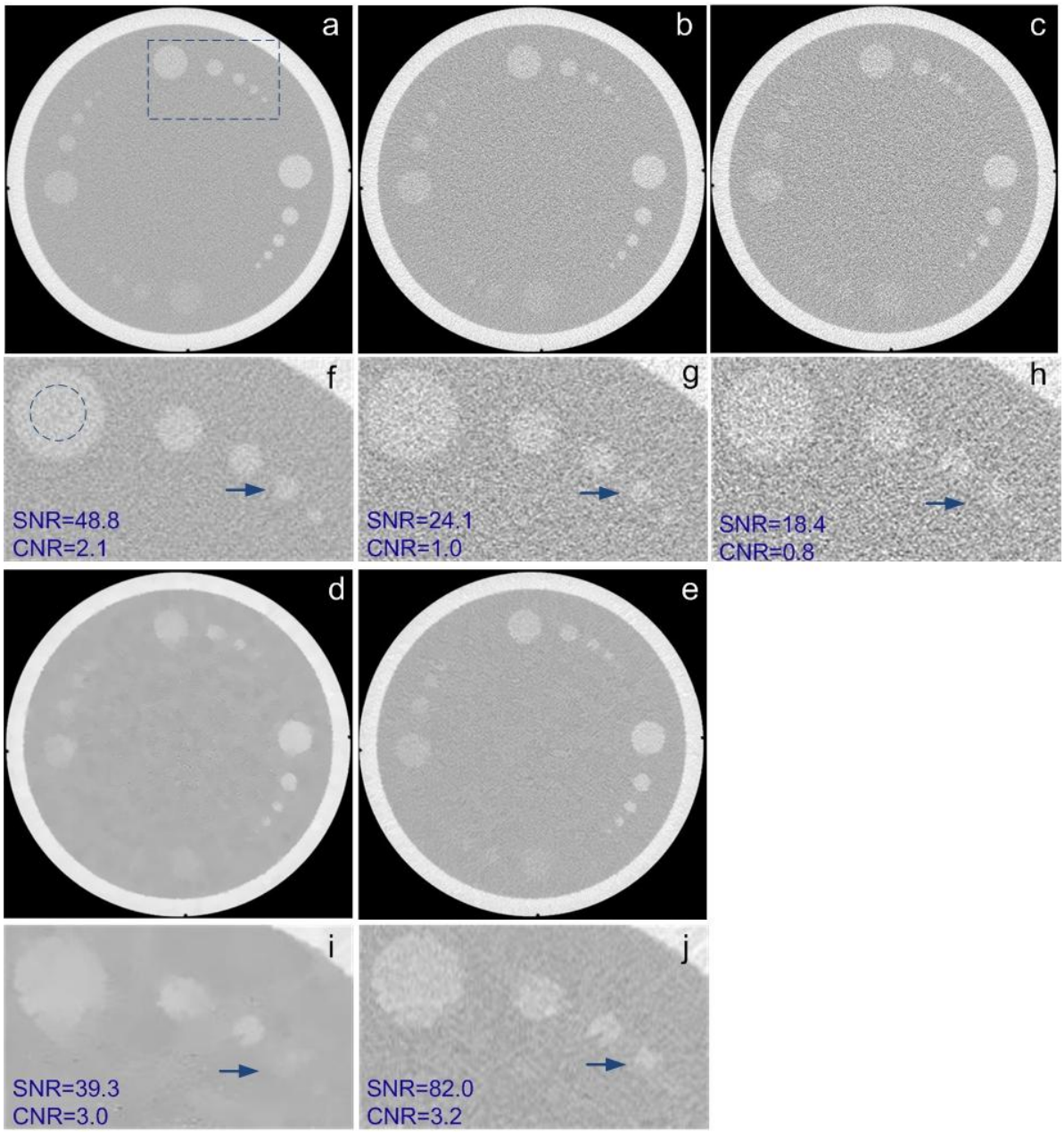

Figure 3.8. Comparative reconstructions of the low contrast insert of EMMA phantom. Gray window: [-200,500] HU (a) 583 mAs FBP, (b) 140 mAs FBP, (c) 39 mAs FBP (d) 39 mAs FBP+NLTV and (e) 39 mAs EST. (f)-(j) Zoomed views of the rectangular region. The 5mm diameter cylinder is indicated by arrows. The SNRs and CNRs of the circled region, labled in (f), were calculated for all the reconstructions.

3.4.2. Spatial Resolution Phantom

We quantified the image spatial resolution of the FBP and EST reconstructions by using the resolution insert of the EMMA phantom. Figs. 3.9 (a-e) show bar groups 10 and 11 in the resolution insert obtained from the 583mAs FBP, 140mAs FBP, 39mAs FBP, 39 mAs FBP+NLTV and 39mAs EST reconstructions, respectively. The standard uncropped ramp filter was used in all the FBP reconstruction in order not to degrade the resolution. The line profiles along the dotted line in Fig. 3.9 (a) are plotted in Fig. 3.9 (f). The smallest bar group 11 (1 line pair per mm) is not clearly differentiable in all reconstruction, but the second smallest bar group 10 (0.8 line pairs per mm with a width of 0.62 mm per bar) is visible in all reconstructions. In contrast to FBP reconstructions at 140 mAs and 39 mAs, in which noise degrades the geometrical fidelity of the bars as sharp rectangular objects, the 39mAs EST reconstruction (Fig. 3.9 (e)) maintains a noise-free appearance similar to the 583mAs FBP reconstruction (Fig. 3.9 (a)). From these results, it can be concluded that incorporating the advanced regularization algorithms in the low flux, low dose setting will not significantly degrade the high contrast resolution.

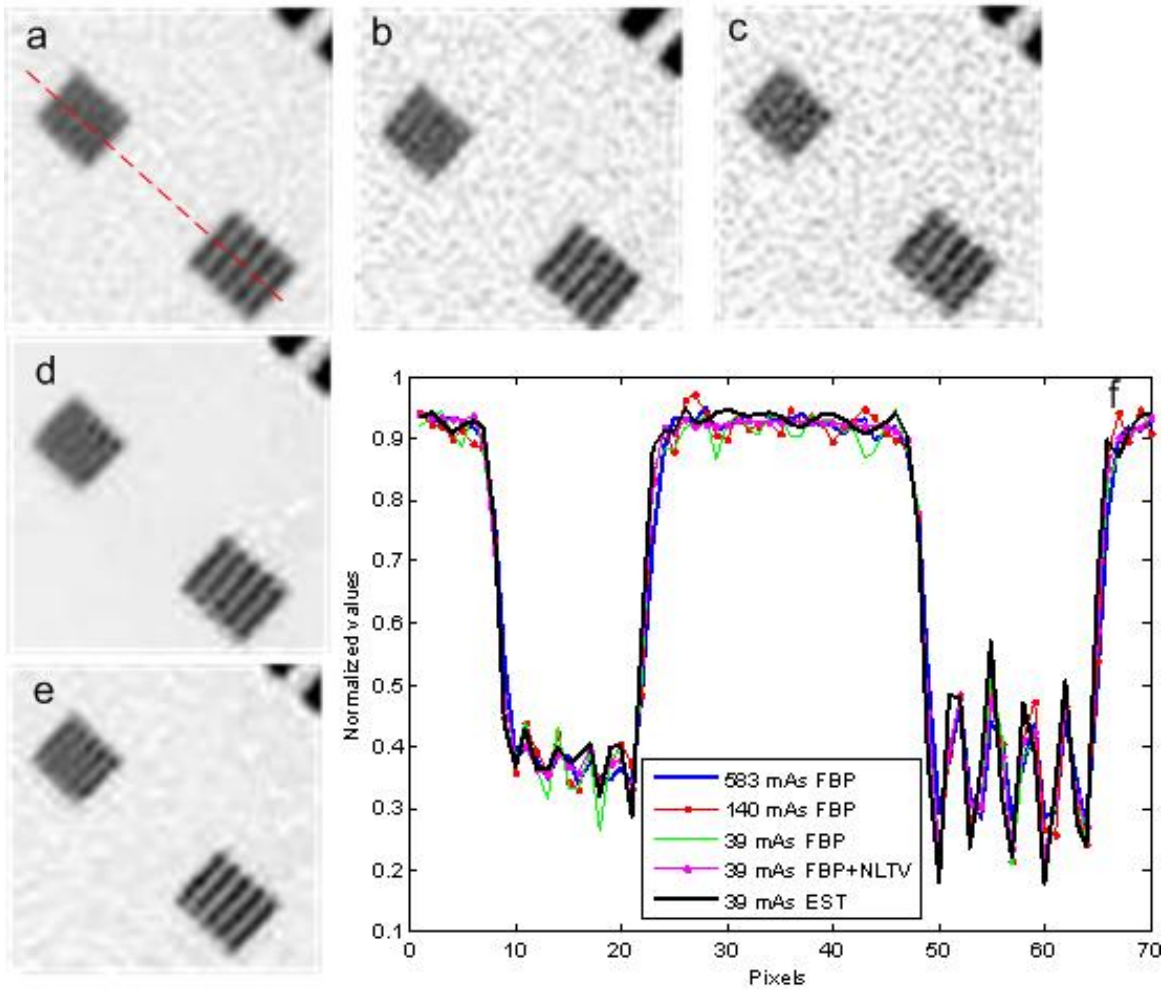

Figure 3.9. Comparative reconstructions of the resolution insert of the EMMA phantom. Gray window: [-200,800] HU. Zoomed images of two smallest bar groups 10 and 11 for the reconstructions of (a) 583 mAs FBP, (b) 140 mAs FPB, (c) 39 mAs FBP, (d) 39 mAs FBP+NLTV and (e) 39 mAs EST. (f) The line profiles along the dotted line in (a) are plotted.

3.4.3. Pediatric Patient Data

Figs. 3.10 and 3.11 show two representative head slice from two different scans from the same anonymous pediatric patient reconstructed by 140 mAs FBP, 39 mAs FBP and 39 mAs EST. Relative to the protocol setting of 140 mAs, the 39 mAs reconstructions simulate with 70% less imaging dose. It is noted that the low-dose EST reconstructions at 39 mAs contains noise characteristics similar to FBP at 140 mAs, while the image quality of the low-dose FBP reconstructions at 39 mAs are degraded by noise. The 39 mAs EST reconstruction still contains most of low-contrast structures while the 39 mAs FBP reconstruction has higher noise. Calculation of the cross-correlation coefficient resulted in a higher correlation for the EST reconstructions in both Figs. 3.10 and 3.11. The low contrast regions indicated by the arrows in 39 mAs EST are in great agreement with the 140 mAs FBP, while its visibility is degraded by the high noise level in 39 mAs FBP. Comparative reconstructions were also performed by using 140 mAs FBP, 39 mAs FBP with NLTV regularization, and 39 mAs EST with the same NLTV regularization parameters (Fig. 3.12). Circled regions indicate the degradation of fine features by simply applying the NLTV regularization to the 39 mAs FBP reconstruction. This evidence further proves that the regularization only is not enough to generate a noise-free image with high contrast and resolution information. The advanced iterative EST algorithm provides a platform for the regularization method, achieves the balance between the noise regularization and the data consistency with real experiments.

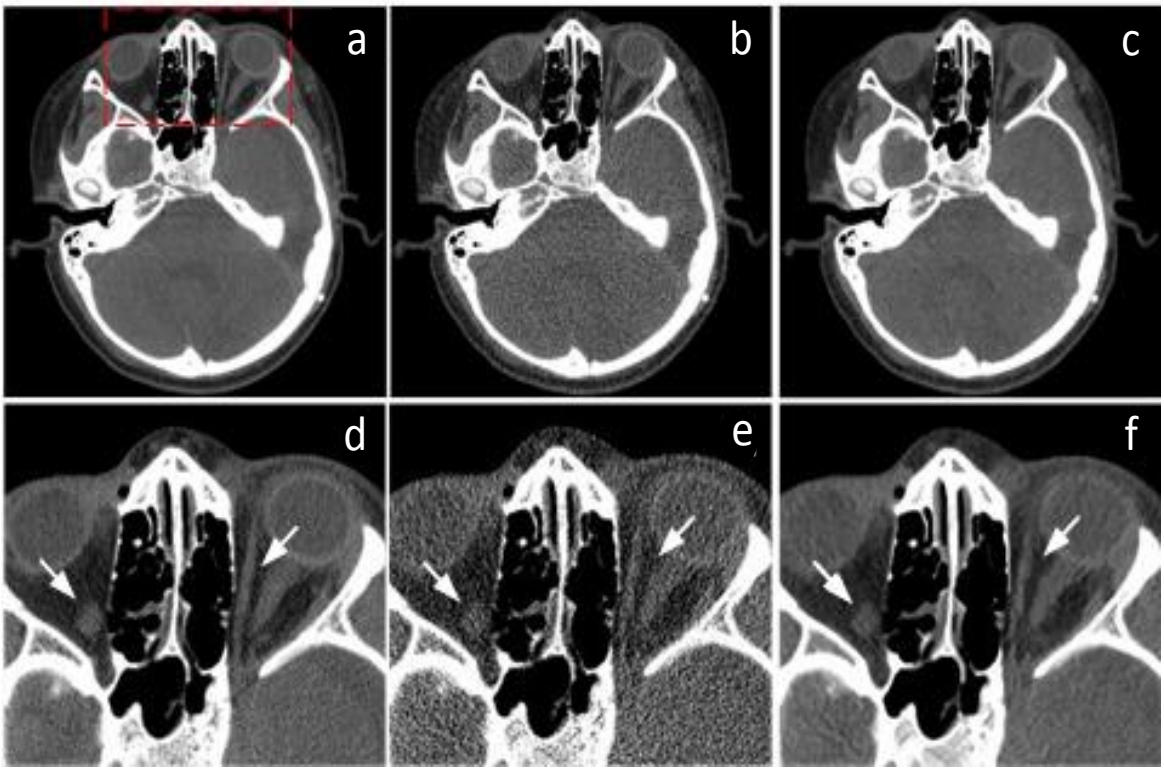

Figure 3.10. Comparative reconstructions of a head slice from a pediatric patient. Gray window: [-400,500] HU. (a-c) Whole slice reconstructions for 140 mAs FBP, 39 mAs FBP, 39 mAs EST. (d-f) The corresponding zoomed images of the rectanglular region with fine and low-contrast structures. The white arrows point to some fine features.

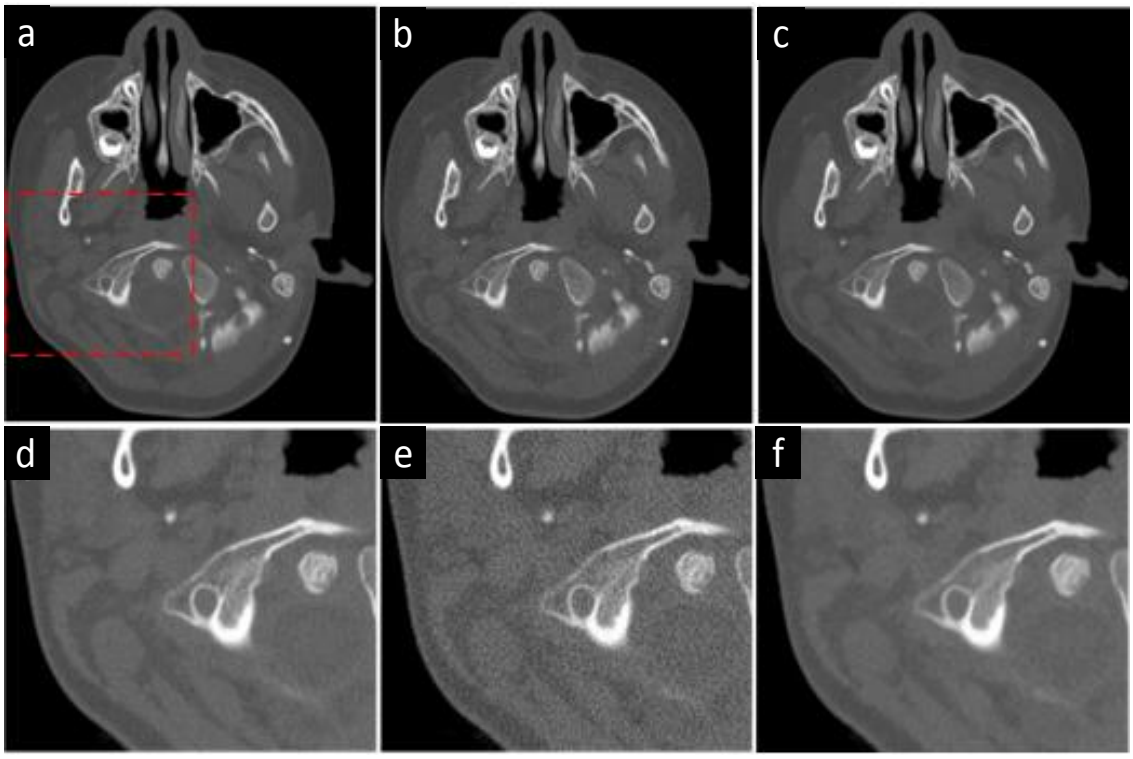

Figure 3.11. Comparative reconstructions of another head slice from the pediatric patient data set. The gray windows for (a-c): [-400,800] HU and for (d-f): [-400,600] HU. (a-c) Whole slice reconstructions for 140 mAs FBP, 39 mAs FBP, 39 mAs EST. (g-l) The corresponding zoomed images of the rectangular region with fine and low-contrast structures.

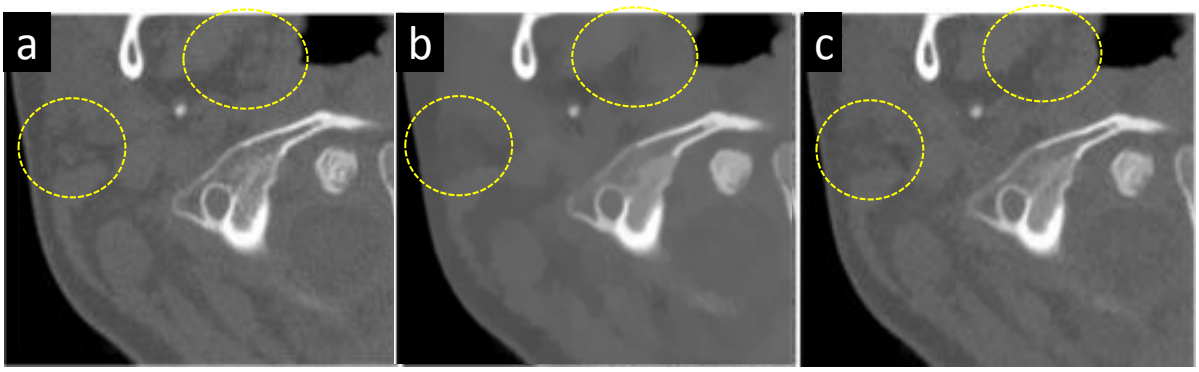

Figure 3.12. The effect of regularization on EST and FBP. Comparative reconstructions by 140 mAs FBP (a), 39 mAs FBP with NLTV regularization (b), and 39 mAs EST with the same NLTV regularization parameters (c). Circled regions indicate the degradation of fine features by simply applying the NLTV regularization to the 39 mAs FBP reconstruction. Grayscale windows: [-400,600] HU.

3.5. Discussion

There is no single metric that can adequately quantify image quality, and in the analysis of image quality and aggregate of metrics, both subjective and objective, must be considered along with purpose of the imaging task. The purpose of this chapter is to address the feasibility of performing low dose reconstructions using an efficient Fourier based algorithm and regularization method. Due to the complexity of the analysis of image quality, in general, one cannot readily derive a specific dose reduction factor in simplistic terms. However, the results in this work demonstrate an enhanced performance of the proposed algorithm, relative to the conventional method, in the realm of low dose fan beam CT. The evaluation utilized is firstly a

comparison to a high dose reconstruction. Accordingly, for the image quality phantom analysis, data sets, acquisitions and reconstructions were made the highest possible flux setting of the scanner at 583 mAs, protocol setting of 140 mAs, followed by EST reconstructions of 39 mAs which deliver 70% lower dose than the protocol 140 mAs. Although equivalence cannot be claimed in such low dose reconstructions due to the complexity of image analysis, it is demonstrated that in both the EMMA imaging quality phantom and a pediatric patient data acquired from a clinical CT scanner, that the 39mAs EST reconstruction produces comparable image quality, resolution and contrast relative to 140mAs FBP reconstruction.

The proposed EST method also provides an efficient way to enforce measured data in Fourier space, which through the PPFFT constitutes an accurate and fast method for calculating the equivalent of forward and back projections. This allows any regularization constraint to be implemented in manner such that the final reconstruction result is strictly consistent with the measured, since in each iteration, including the final step of the iterative algorithm, the measured data is reinforced data in Fourier space. This is to be contrasted by a method that simply applies denoising or regularization to FBP reconstructions, as by doing so, there is no guarantee that the final image is consistent with patient measurements, or that over-smoothing and loss of important features have not occurred. To demonstrate this more thoroughly, the NLTV regularization was simply applied to the FBP reconstructions in both the phantom and patient data. As expected, the high contrast resolution is not considerably affected by such a procedure; however the fine contrast features, such as those shown Figs. 10 and 11 by the arrows are degraded. Fig. 12 shows a comparison of regions for the pediatric patient data using NLTV with

the exact same parameters as the EST algorithm, which demonstrate that some structures (shown in dashed circles) are lost if such a simple method is attempted.

References

1. A.C. Kak, and M. Slaney, *Principles of Computerized Tomographic Imaging*. (SIAM, Philadelphia, 2001).
2. G. T. Herman, *Fundamentals of Computerized Tomography: Image reconstruction from projection*, 2nd ed. (Springer, New York, 2009).
3. J. Hsieh, "*Computed Tomography: Principles, Design, Artifacts, and Recent Advances*," 2nd ed. (Wiley, Washington, 2009).
4. T. M. Buzug, *Computed Tomography: from photons statistics to modern cone-beam CT*. (Springer, Berlin, 2008).
5. A. Berrington de Gonzalez, et al. "Projected cancer risks from computed tomographic scans performed in the United States in 2007," Arch. Intern. Med. **169**, 2071-2077 (2009).
6. R. Smith-Bindman, et al. "Radiation dose associated with common computed tomography examinations and the associated lifetime attributable risk of cancer," Arch. Intern. Med. **169**, 2078-2086 (2009).
7. R.H. Fazel, et al. "Exposure to low-dose ionizing radiation from medical imaging procedures," N. Engl. J. Med. **361**, 849-857 (2009).
8. A.J. Einstein, et al. "Radiation dose and cancer risk estimates in 16-slice computed tomography coronary angiography," J. Nucl. Cardio. **15**, 232-240 (2008).

9. S. Kim, T.Yoshizumi, D.P. Frush, G. Toncheva, F.F. Yin, "Radiation dose from cone beam CT in a pediatric phantom: risk estimation of cancer incidence," AJR Am J Roentgenol. **194**, 186-190 (2009).
10. Annual report from the National Council on Radiation Protection & Measurements. <www.ncrponline.org/PDFs/NCRP_2009_Ann_Report.pdf> (2009).
11. E. Candes, J. Romberg, T. Tao, "Exact signal reconstruction from highly incomplete frequency information," IEEE Trans. Inf. Theory. **52**, 489–509 (2006).
12. G.H. Chen, J. Tang, and S. Leng, "Prior image constrained compressed sensing (PICCS): a method to accurately reconstruct dynamic CT images from highly undersampled projection data sets," Med. Phys. **35**(2), 660-3, (2008).
13. E.Y. Sidky, and X. Pan, "Image reconstruction in circular cone-beam computed tomography by constrained, total-variation minimization," Phys. Med. Biol. **53**(17), 4777-807, (2008).
14. H. Yu, and G. Wang, "Compressed sensing based interior tomography," Phys. Med. Biol. **54**(9), 2791–2805, (2009).
15. G.H. Chen, et al., "Temporal resolution improvement using PICCS in MDCT cardiac imaging," Med. Phys. **36**(6), 2130-35 (2009).
16. J.C. Ramirez-Giraldo, et al., "Nonconvex prior image constrained compressed sensing (NCPICCS): Theory and simulations on perfusion CT," Med. Phys, **38**(4), 2157-67 (2011).
17. L. Ritschl, et al, "Improved total variation-based CT image reconstruction applied to clinical data," Phys. Med. Biol. **56**(6), 1545-61(2011).
18. L.A. Feldkamp, L.C. Davis, and J.W. Kress, "Practical cone-beam algorithm," J. Opt. Soc. Am. B: Opt. Phys. 1(6), 612-9, (1984).

19. Y. Kyriakou, M. Kachelriess, M. Knaup, J.U. Krause, W.A. Kalender, "Impact of the z-flying focal spot on resolution and artifact behavior for a 64-slice spiral CT scanner," Eur. Radiol. 16, (6), 1206-15, (2006).
20. Kachelriess, M., S. Schaller, and W.A. Kalender, Advanced single-slice rebinning in cone-beam spiral CT. Med Phys, 2000. 27(4): p. 754-72.
21. A. H. Delaney and Y. Bresler, "A fast and accurate Fourier algorithm for iterative parallel-beam tomography". IEEE Trans. Im. Proc., **5**(5):740-53(1996).
22. S. Matej, J.A. Fessler, I.G. Kazantsev, "Iterative tomographic image reconstruction using Fourier-based forward and back-projectors," IEEE Trans. Med. Imaging. **23**, 401-412 (2004).
23. Y. Zhang-O'Connor and J.A. Fessler, "Fourier-based forward and back-projectors in iterative fan-beam tomographic image reconstruction," IEEE Trans. Med. Imag. **25**, 582-9 (2006).
24. W.L. Briggs and V.E. Henson, *The DFT: an owner's manual for the discrete Fourier transform.* 3rd ed. (SIAM, Philadelphia, 1995).
25. R.M. Mersereau and A.V. Oppenheim, "Digital reconstruction of multidimensional signals from their projections," Proc. IEEE. 62 1319–38 (1974).
26. A. Averbuch, et al., "A Framework for Discrete Integral Transformations I—The Pseudopolar Fourier Transform," SIAM Journal on Scientific Computing. **30**(2), 785-803, (2008).
27. D.H. Bailey, and P.N. Swarztrauber, "The fractional Fourier transform and applications," SIAM Review. 33(3), (1991).
28. J. Miao, F. Förster, O. Levi, "Equally sloped tomography with oversampling reconstruction," Phys. Rev. B. 72, 052103 (2005).

29. J. Miao, C.C. Chen, C. Song, Y. Nishino, Y. Kohmura, T. Ishikawa, D. Ramunno-Johnson, T.K. Lee, S.H. Risbud, "Three-Dimensional GaN-Ga_2O_3 Core Shell Structure Revealed by X-ray Diffraction Microscopy", Phys. Rev. Lett. **97**, 215503 (2006).
30. E. Lee, B.P. Fahimian, C.V. Iancu, C. Suloway, G.E. Murphy, E.R. Wright, D. Castaño-Díez, G.J. Jensen, and J. Miao, "Radiation dose reduction and image enhancement in biological imaging through equally-sloped tomography," J. Struct. Biol. **164**(2), 221-227, (2008).
31. Y. Mao, B.P. Fahimian, S. Osher, J. Miao, "Development and Optimization of Regularized Tomographic Reconstruction Algorithms Utilizing Equally-Sloped Tomography," IEEE Trans Image Process. **19**(5), 1259 – 1268, (2010).
32. B.P. Fahimian, Y. Mao, P. Cloetens, J. Miao, "Low dose x-ray phase-contrast and absorption CT using Equally-Sloped Tomography," Phys. Med. Biol. 55, 5383-5400 (2010).
33. H. Jiang, C. Song, C.-C. Chen, R. Xu, K.S. Raines, B.P. Fahimian, C. Lu,. T.-H. Lee, A. Nakashima, J. Urano, T. Ishikawa, F. Tamanoi, J. Miao, "Quantitative 3D Imaging of Whole, Unstained Cells by Using X-ray Diffraction Microscopy," Proc. Natl. Acad. Sci. USA. 107, 11234–11239 (2010).
34. M. C. Scott, C.-C. Chen, M. Mecklenburg, C. Zhu, R. Xu, P. Ercius, U. Dahmen, B. C. Regan, J. Miao, " Electron tomography at 2.4 Å resolution," Nature 483, 444-447(2012).
35. Y. Zhao, E. Brun, P. Coan, Z. Huang, A. Sztrókay, P. C. Diemoz, S. Liebhardt, A. Mittone, S. Gasilov, J. Miao, A. Bravin, "High resolution, low dose phase contrast x-ray tomography for 3D diagnosis of human breast cancers", Proc. Natl. Acad. Sci. USA, under review.

36. J. Miao, P. Charalambous, J. Kirz and D. Sayre, "Extending the methodology of X-ray crystallography to allow imaging of micrometre-sized non-crystalline specimens," Nature. 400, 342-344 (1999).

37. J. Miao, T. Ishikawa, T. Earnest, Q. Shen, "Extending the Methodology of X-ray Crystallography to Allow Structure Determination of Non-Crystalline Materials, Whole Cells and Single Macromolecular Complexes," Annu. Rev. Phys. Chem. 59, 387–409 (2008).

38. K.S. Raines, S. Salha, R.L. Sandberg, H. Jiang, J.A. Rodríguez, B.P. Fahimian, H.C. Kapteyn, J. Du and J. Miao, "Three-dimensional structure determination from a single view," Nature. 463, 214-217 (2010).

39. S. Osher, M. Burger, D. Goldfarb, J. Xu, W. Yin, "An iterative regularization method for total variation-based image restoration," Multiscale Model Simul. **4**, 460-489 (2005).

40. A. Buades, B. Coll, J.M. Morel, "A review of image denoising algorithms, with a new one," Multiscale Model. Simul. **4**, 490–530 (2005).

41. G. Gilboa and S. Osher, "Nonlocal operators with applications to image processing," Multiscale Model. Simul. **7**, 1005–1028 (2008).

42. O. Gayou, M. Miften, "Commissioning and clinical implementation of a megavoltage cone beam CT system for treatment localization" Med. Phys. **34**, 3183-92 (2007).

43. P. Massoumzadeh, et al., "Validation of CT dose-reduction simulation," Med. Phys. **36**(1) 174-89 (2009).

44. B.R. Whiting, et al., "Properties of preprocessed sinogram data in x-ray computed tomography," Med. Phys. **33**(9), 3290-303 (2006).

CHAPTER 4

LOW DOSE X-RAY PHASE CONTRAST MAMMOGRAPHY CT RECONSTRUCTION OF THROUGH EQUALLY SLOPED TOMOGRAPHY

4.1. Introduction

Human breast cancer is a type of cancer originating from breast tissue. Worldwide, breast cancer comprises 22.9% of all cancers (excluding non-melanoma skin cancers) in women. (1) In 2008, breast cancer caused 458.503 deaths worldwide (13.7% cancer deaths in women). The cure and survival rates of breast cancer greatly depend on the cancer type and staging (1), which is directly related to the accuracy of screening and diagnosis techniques. Mammography is now the primary imaging tool for early detection of breast cancers. While more advanced technologies such as digital mammography have been developed to improve its image quality (2), there are three potential risks associated with mammography. First, mammograms miss up to 20% of breast cancers that are present during the time of screening (3). Second, in some cases mammograms appear abnormal, but no breast cancers are actually present (4). Third, repeated mammography examinations have the potential of causing cancers (5). Dedicated breast computed tomography (CT) can reduce some of these risks, but its spatial resolution (~400 μm) is mainly limited by the x-ray dose deliverable to the radiation-sensitive human breast and its detection of micro-calcifications is inferior to mammography (6). Furthermore, some tumours

are not visible in CT because its image contrast is based on the x-ray absorption coefficients and is intrinsically low between tumours and normal tissues.

To improve the future detection accuracy while further reducing the radiation dose for human breast cancer screening and diagnostics, we combined the "phase contrast x-ray tomography (PCT)" with our EST reconstruction algorithm; performed experiment with a whole human breast sample with an invasive ductal cancer. This approach has been demonstrated as a high resolution, high contrast and low dose PCT method.

4.2. Methods

4.2.1. Phase Contrast X-ray CT

The behavior of x-rays as they travel through an object can be described in terms of a complex index of refraction n, of which the real part (δ) and the imaginary part (β). The relations between n, δ and β can be expressed as:

$$n = 1 - \delta - i\beta \qquad (Eq. 4.1)$$

$$\delta = \frac{r_c \lambda^2}{2\pi} \rho \qquad (Eq. 4.2)$$

$$\beta = \frac{\lambda}{4\pi} \mu \qquad (Eq. 4.3)$$

Where r_c, λ, ρ and μ represent classical electron radium, x-ray wave length, electron density and the linear absorption coefficient. δ represents the x-ray absorption by the object while β represents the phase shift (refraction). The ratio of δ and β is determined by:

$$\frac{\delta}{\beta} = \frac{2r_c\rho\lambda}{\mu} \qquad (Eq.\,4.4)$$

For some low Z material such as biological soft tissue, as indicated in equation 4, the variation of the linear attenuation coefficients is typically on the order of 0.1-0.3 cm^{-1} in the x-ray energy range of 10-60 keV (7) that is commonly used in radiology. As a result, the image contrast based on x-ray absorption may not be sufficiently high enough to image the normal and diseased tissues in a sample. Compared to the x-ray absorption, the phase shift in the hard x-ray energy range is two to three orders of magnitude higher (8). Therefore, radiographic techniques that are sensitive to the variation of the phase shift can significantly enhance the image contrast relative to the x-ray absorption based techniques. Over the past few decades, phase contrast x-ray imaging has been under rapid development and various methods for detecting the refracted x-rays have been implemented (9-18). However, presently two of the major challenges prevent PCT from becoming an in vivo imaging tool for clinical application. First, in order to achieve high resolutions (i.e. tens of microns) for accurate diagnosis, PCT requires several thousands of projections from a whole human breast. The total radiation dose delivered to the breast is thus higher than that in dual-view mammography. Second, PCT uses sophisticated x-ray optics and the acquisition time for several thousands of projections is usually too long for clinical application.

4.2.2. Equally Sloped Tomography for Phase Contrast CT

EST reconstruction algorithm, because of its characteristic of utilizing much fewer number of projections to achieve higher contrast and higher resolution images, can overcome the over dose and long data acquisition time problem of PCT while fully addressing the advantage of contrast performance of PCT.

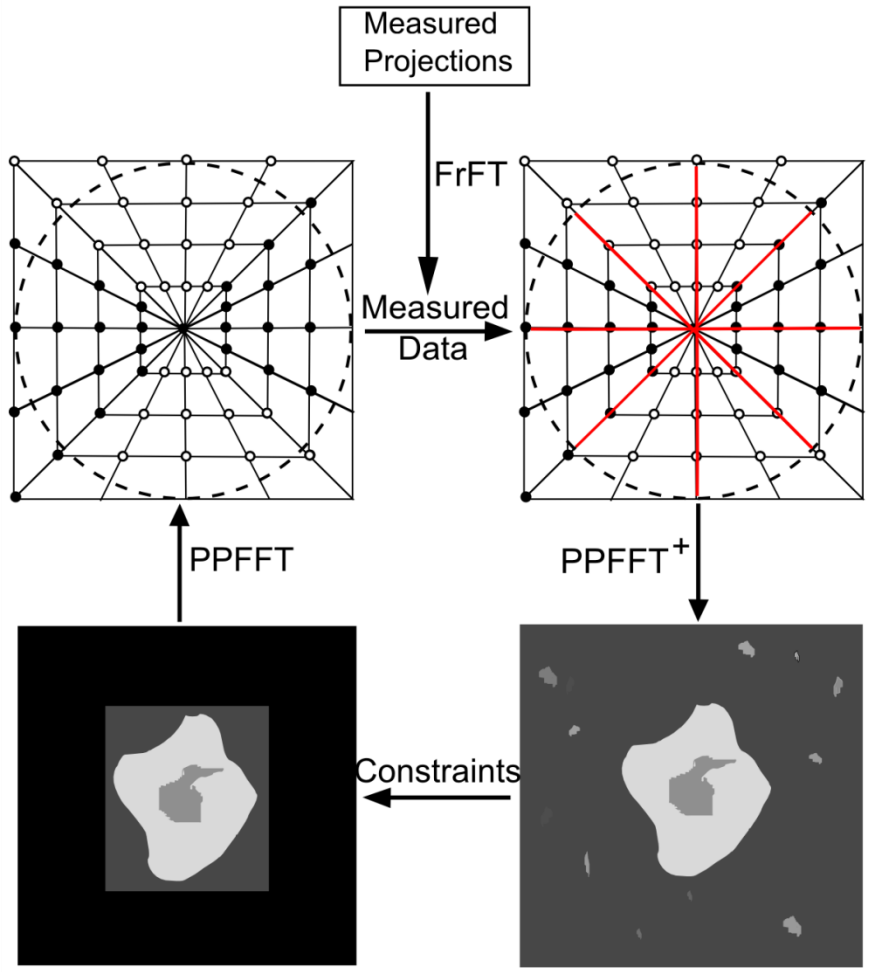

Figure. 4.1. Schematic layout of the iterative EST algorithm for Phase contrast CT.

Unlike conventional CT reconstruction methods, EST utilizes a pseudo-polar grid and the pseudo-polar fast Fourier transform (PPFFT) as addressed before. The algorithm starts with padding each projection with zeros and calculating its oversampled Fourier slice in the pseudo-polar grid (red lines in Fig. 4.1 top-right). The grid points outside the resolution circle (the circle with dashed lines in Fig. 4.1) and on the missing projections (black lines in Fig. 4.1 top-right) are set to zero. The algorithm iterates back and forth between real and Fourier space by the following steps (19-23).

i) A real-space image is obtained (Fig. 4.1 bottom-right) by applying the adjoint PPFFT to the Fourier-space slices. Here the adjoint PPFFT instead of the inverse PPFFT is used because the former is implemented through a conjugate gradient method and can be computed much faster than the latter without compromising the accuracy (22).

ii) A support is determined from the image based on the zero padding of the projections. Outside the support the voxel values are set to zero, and inside the support the negative values are set to zero. A new image is obtained (Fig. 4.1 bottom-left).

iii) By applying the PPFFT to the new image, an updated set of Fourier-space slices is obtained (Fig. 4.1 top-left).

iv) Those Fourier slices corresponding to red lines in Fig. 4.1 are replaced with the measured ones, while the grid points outside the resolution circle and on the missing Fourier slices (i.e. black lines) remained unchanged. The revised set of the Fourier slices is used for the next iteration.

v) An error metric is calculated to monitor the convergence of the algorithm, defined as normalized difference between the measured and calculated Fourier slices.

In this experiment, the algorithm was automatically terminated when the error became stabilized after about 20 iterations.

After the iteration process was finished, a non-local means technique was applied to the reconstructed image (27). This technique has proven to be effective in removing noise while preserving edge contrasts. In our case the non-local means filter was carefully set to partially eliminate noise but not fine structures.

4.2.3. Experiment setup

The experiment was conducted on the biomedical beamline at the European Synchrotron Radiation Facility (ESRF) (24). The sample was a human breast mastectomy specimen (~9.5 cm in diameter) issued from a 75-year-old woman with an invasive ductal cancer and fixed in 4% formalin. The reason that we chose an invasive ductal carcinoma is because it is the most frequent breast cancer entity. The study was conducted in accordance with the Declaration of Helsinki and was approved by the local ethics committee. A collimated x-ray beam with energy of 60 keV was monochromatized by a double Si (111) crystal system and an additional single Si (333) crystal (Fig. 4.2). The use of high energy x-rays (60keV) was justified to reduce the radiation dose to the sample and allow for the imaging of thick tissues. The breast cancer sample

was mounted on a rotary stage and placed in the x-ray beam. The refracted and scattered x-rays by the sample were analyzed by a Si (333) perfect silicon analyzer crystal. The analyzer crystal acts as an extremely narrow slit which can select with extremely high sensitivity ($\approx 10^{-6}$ rad) the x-rays exiting the sample. It was rotated according to the incoming x-ray beam and set at an angle close to the Bragg diffraction condition. After each rotation, the sample was vertically displaced relative to the x-ray beam, allowing a different region to be imaged. A 60 μm thick Gadox fluorescent screen was used to convert the x-rays into visible light to be recorded by the fast readout and low noise 2048 x 2048 pixel charge coupled device (CCD). The image were taken with a 2 x 2 binning in order to have an effective 92 x 92 μm pixel size, which sets the spatial resolution of the imaging technique. The total acquisition time is ~25.1 minutes.

The image contrast of this experimental set-up is determined by the rocking curve (RC) of the analyzer crystal. The analyzer modulates the beam by converting the small angular change of the x-ray propagation to the intensity variation on the detector. Depending on the position of the analyzer crystal, the image contrast varies because the Bragg condition is fulfilled by the refracted and scattered x-rays at different angles from the sample. In this study, we set the position of the analyzer about 40% to the left of the rocking curve peak. The phase contrast x-ray images were measured by a fast-readout and low-noise CCD detector (25).

To achieve high spatial resolution in conventional PCT, the number of projections (N) required is determined by $N \sim \pi D/(2P)$ where D is the thickness of the sample and P the detector pixel size. In this experiment, 2000 projections from 0 ~ 180 degrees with a increment of 2000/180 degree

were measured from the whole breast cancer sample. Although the acquired projections are a mixture of the x-ray absorption, refraction and scatter effects, the application of CT reconstruction methods remains valid due to the small refraction angle approximation for soft tissues (26).

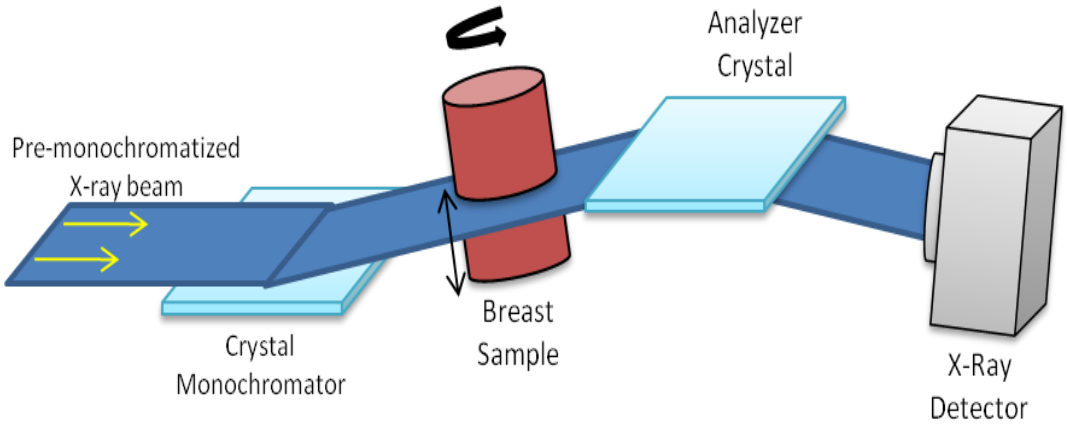

Figure 4.2. Schematic diagram of the phase contrast X-ray imaging setup. A collimated x-ray beam with energy of 60 keV was monochromatized by a double Si (111) crystal system and an additional single Si (333) crystal. The breast cancer sample was mounted on a rotary stage and placed in the x-ray beam. The refracted and scattered x-rays by the sample were analyzed by a Si (333) analyzer crystal. The analyzer crystal was rotated according to the incoming x-ray beam and set at an angle close to the Bragg diffraction condition. After each rotation, the sample was vertically displaced relative to the x-ray beam, allowing a different region to be imaged. A fast readout and low noise charge coupled device (CCD) camera with 2048 x 2048 pixels was used to measure the phase contrast x-ray images.

4.2.4. Evaluation Methods

We performed the conventional PCT reconstruction of the whole breast cancer sample from 2000 projections using the gold-standard filtered back projection (FBP) with a Hamming filter (28). The same volume was computed with the EST reconstruction using 512 out of the 2000 projections. For a comparison purpose, a FBP reconstruction was also computed with 512 projections. In order to explore the limit of the EST method and investigate the possibility of further reducing the radiation dose and the acquisition time, we also performed an EST reconstruction with only 200 projections. For FBP reconstruction, equally-angled acquisition is maintained after we manually removed the number of projections from 2000 to 512. The angle increments in these cases are 512/180. For EST reconstruction, since equally-sloped acquisition is desired, we performed nearest neighbor interpolation to achieve the projections at 512 and 200 cases.

Both human study and quantitative comparisons were performed on the reconstructed images for performance evaluation. For the four sets of reconstructions (FBP 2000 projections, EST 512 projections, FBP 512 projections and EST 200 projections), two sets of images (one set for axial view and one set for sagittal view) were selected and blindly examined by five independent and experienced radiologists. The images from different reconstruction conditions were mixed and disordered on purpose and displayed to the radiologists. Based on the current clinical image evaluation systems, in an attempt to standardize image evaluation in conventional mammography, the American College of Radiology (ACR) and the European Commission (EU)

have published guidelines which include characteristics for image quality control (29). The ACR guidelines include *positioning of the breast, compression, exposure level, contrast, sharpness, noise* and *artifacts.* The EU guidelines comprise amongst others: *sharp reproduction of glandular tissue, retroglandular fat tissue, visualization of skin outline* and *reproduction of vascular structures, vessels, fibrous strands and skin structure*. These criteria were summarized as "*evaluation of different structure*". The different tumour borders, skin layers, fatty tissues and collagen strands were easily identified by the radiologists. To make the evaluation quantitative, five criteria were adopted by the radiologists based on current clinical image evaluation systems as mentioned. The criteria include i) overall image quality, ii) image sharpness, iii) image quality, iv) evaluation of different structure, and v) noise level. We also added the criterion of "overall image quality" as a summary of all these criteria. They were evaluated in a range from 1 to 5 (1 being the worst and 5 the best). For quantitative measurements, histogram curves for different reconstruction cases were plotted and compared. Line profile plottings along some fine features in the reconstructions were also compared to evaluate the image resolution and contrast performance of different reconstruction conditions.

4.2.5. 3D Tumour Segmentation Method

Because of the limitation of radiation dose, most conventional mammography techniques take only two projections at different angles. This greatly enhances the difficulty of tumour especially early stage tumour detection and localization. But with the breakthrough of our PCT image technique combining with EST reconstruction algorithm, three dimensional whole tumour

segmentation and detection become possible. In our study, the tissue segmentation on the EST 512 reconstruction has been performed using a segmentation method based on 3D marker-controlled viscous watershed transform (30). This method is well adapted for the intrinsic nature of the PCT images which are characterized by a strong signal at the borders of each feature. The algorithm computes the gradient of the image, some points that belong to the tumour and others belonging to the exterior were selected manually, and then a flooding simulation by a viscous fluid was performed. Results of the flooding are a labeling of all pixels of the images belonging to the tumour. The segmentation results were confirmed and consistent with trained radiologist's interpretation.

4.3. Results

4.3.1. 2D visualization

Both axial and saggital views of the three dimensional reconstruction volume was compared between conventional PCT and EST reconstruction algorithm. Fig. 4.3 shows the same axial slice of the FBP 2000, EST 512, FBP 512 and EST 200 projections reconstructions, separately. The zoomed views of the breast tumour region are shown in Fig. 4.3 (e~h). Visually, the EST 512 reconstruction looks very consistent with FBP 2000 projections, while FBP 512 exhibits high noise, degraded features (indicated by the white arrows) and blurred boundary of the tumour. When pushing the limit to 200 projections, as shown in Fig. 4.3 (f) and (h), though the image quality is limited by the extremely low projection number, the fine features indicated by

the arrows can still be preserved better compared to FBP 512 projections. To better quantitatively visualize the result, Fig 4.4 shows the histograms of the axial slices of the reconstructions in Fig. 4.3 (a~d). It is clear that compared to FBP 2000, EST 512 shows most similarity value distribution. The peak of the histogram for EST 200 degrades compared to FBP2000 and EST 512 but still outperforms FBP 512. The higher noise level in FBP 512 spreads out the curve of histogram and blurs the reconstructed image.

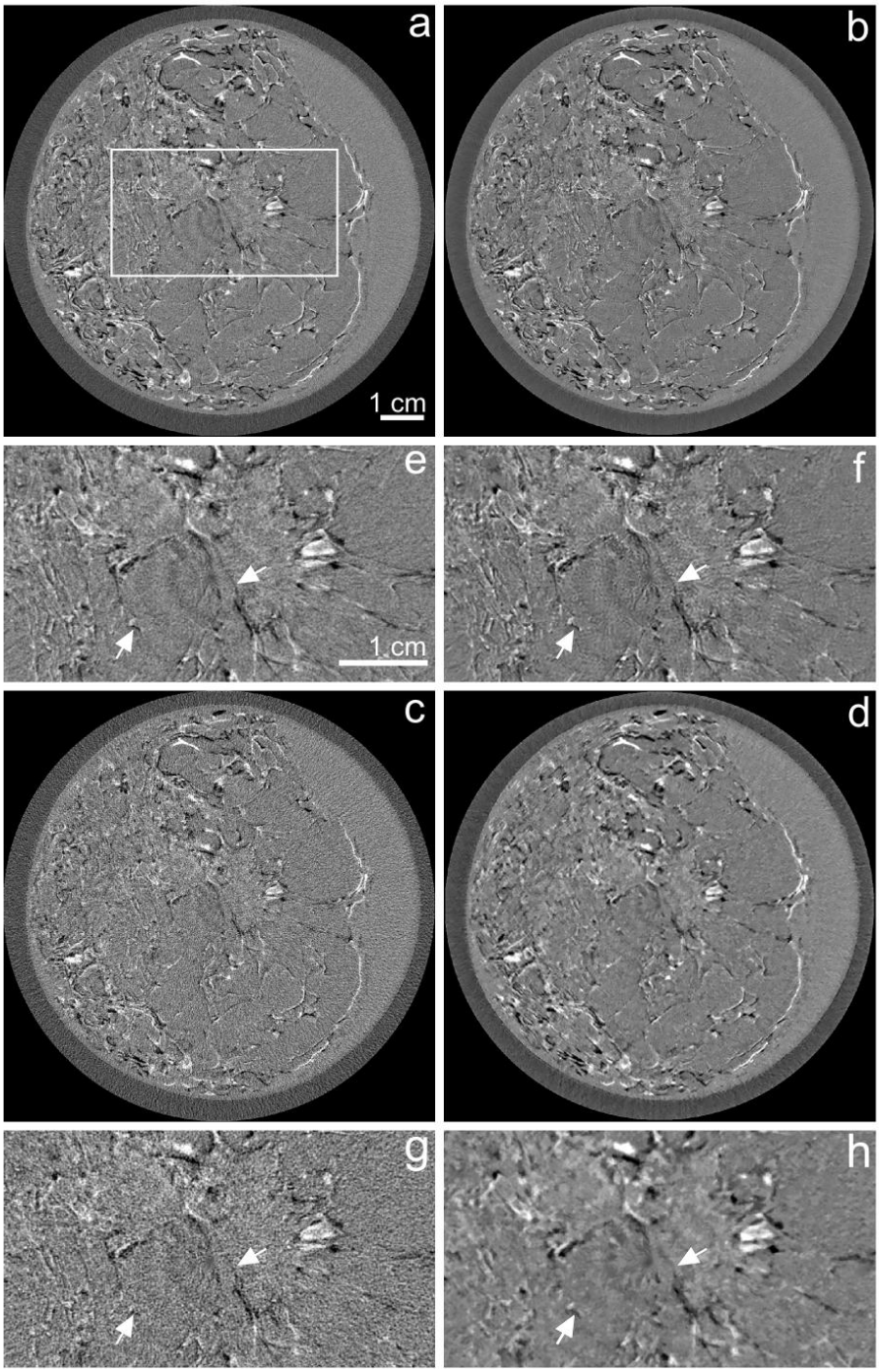

Figure 4.3. Comparison reconstructions of human breast sample using EST and FBP with various numbers of projections. A 92 μm thick axial slice reconstructed by (**a**) FBP 2000, (**b**) EST 512, (**c**) FBP 512 and (**d**) EST 200, in which the white rectangle indicates a tumour region.

Zoomed view of the tumour region (the white rectangle) reconstructed by (**e**) FBP 2000, (**f**) EST 512, (**g**) FBP 512 and (**h**) EST 200, in which the white arrows indicate the visibility of detailed features inside the tumour regions. A Hamming filter was used in the FBP reconstructions, while a non-local means filter was applied to the EST reconstructions.

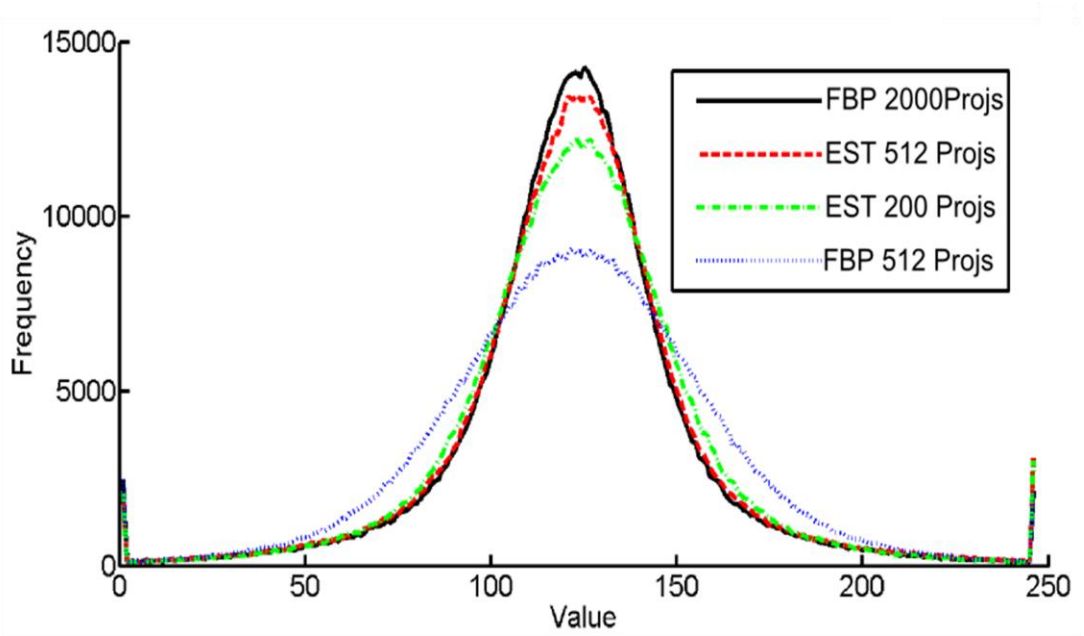

Figure 4.4. Comparison of histogram plots of the reconstructed axial slices between EST and FBP with various numbers of projections. The plots corresponding to Fig 3 a~d from FBP 2000 projections, EST 512 projections, EST 200 projections and FBP 512 projections.

The same saggital slice of the reconstruction volume from FBP 2000 projections, EST 512 projections, FBP 512 projections and FBP 200 projections were compared in Fig. 4.5. The white rectangular in Fig. 4.5 indicates the tumour region. All the fine details in FBP 2000 can be seen

in EST 512, but later utilized only about one quarter number of projections and one quarter of the radiation dose. On the other hand, visually FBP 512 shows significant higher noise level all over the whole image compared to EST 512. The noise blurs the high resolution tissues and degrades the contrast. Fig. 4.6 shows the similar comparison results of another slice from saggital view. To better visualize the resolution performance of EST reconstruction, Fig. 4.7 (b~e) show the zoomed in views of the tumour region in Fig. 4.6 from FBP 2000 projections, EST 512 projections, FBP 512 projections and EST 200 projections. The white arrows point out some small features in the images. It can be seen that the same features can be visualized clearly in FBP 2000, EST 512 and even EST 200, but the high resolution lines and boundaries are blurred or hard to detect in FBP 512. To better compare the resolution performance in a quantitative way, the line profiles along the dashed white line in Fig. 4.7 (a) in all four reconstructions are shown in Fig. 4.7 (f). From the plotting, EST 512(red) fits FBP 2000 (black) closely in all maximum, minimum values and curves, while significant difference can be seen between FBP 2000 and FBP 512. This demonstrates the conventional PCT reconstruction algorithm cannot recover fully resolution information when using less number of projections while our advance EST algorithm can still keep the high resolution information in the reconstructed images.

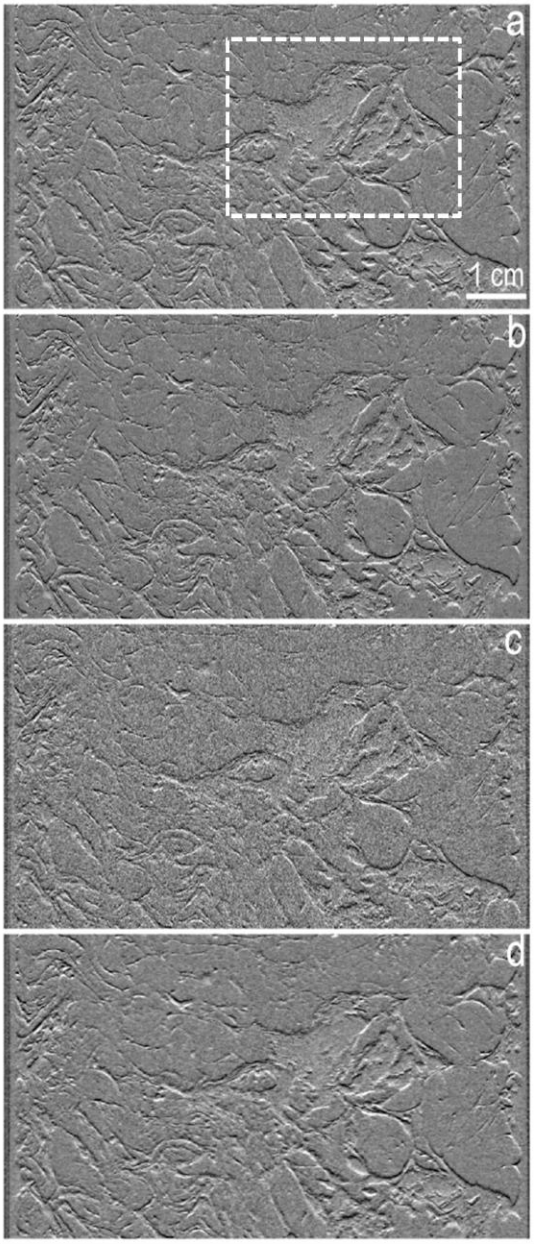

Figure 4.5. Comparison reconstructions of a 92 μm thick saggital slice using FBP and EST with various numbers of projections. The slices were reconstructed by (**a**) FBP 2000, (**b**) EST 512, (**c**) FBP 512 and (**d**) EST 200, in which the white rectangular indicate the tumour region. A Hamming filter was used in the FBP reconstructions, while a non-local means filter was applied to the EST reconstructions.

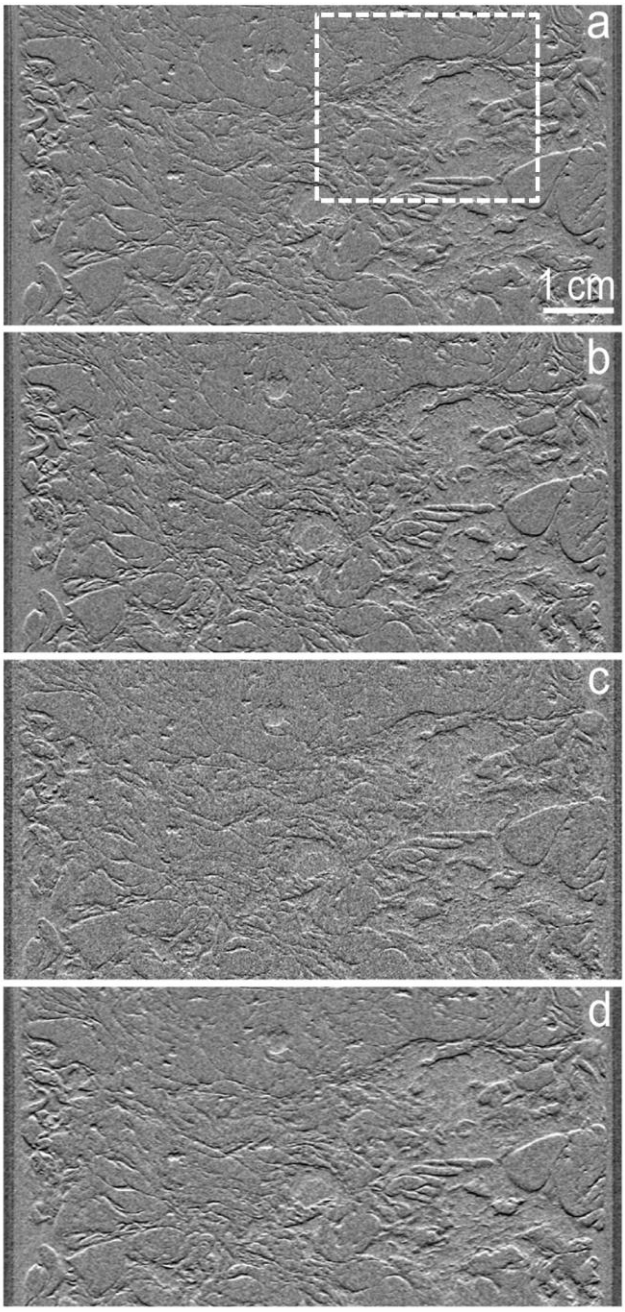

Figure 4.6. Comparison reconstructions of another saggital slice using FBP and EST with various numbers of projections. Another 92 μm thick saggital slice reconstructed by (**a**) FBP 2000, (**b**) EST 512, (**c**) FBP 512 and (**d**) EST 200, in which the white rectangular indicate the tumour region.

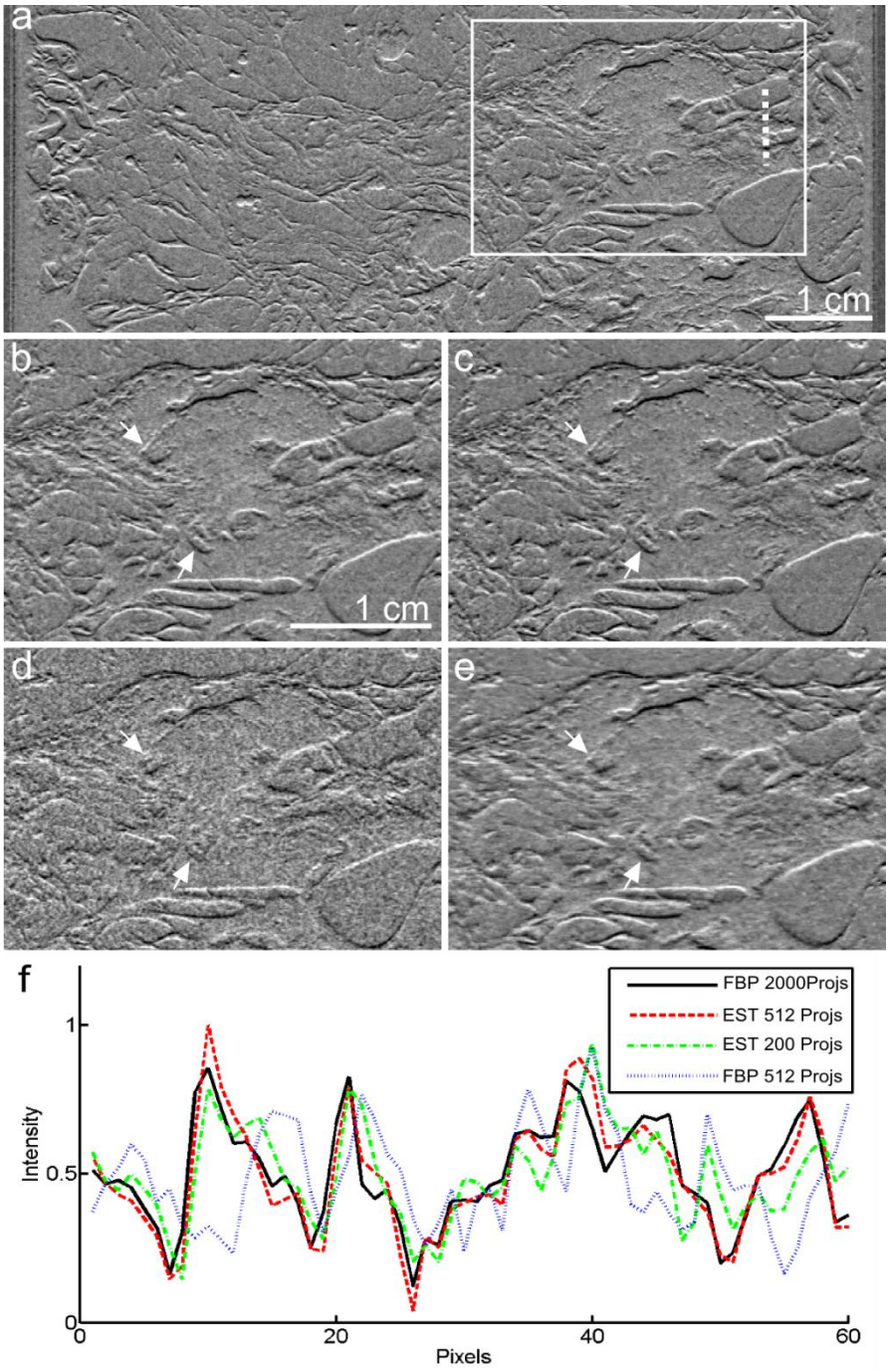

Figure 4.7. Reconstruction comparisons between the conventional PCT and EST reconstructions. (a), A 92 μm thick saggital slice of the FBP 2000 reconstruction, in which the rectangle indicates a tumour region. Zoomed view of the tumour region reconstructed by FBP

2000 (b), EST 512 (c), FBP 512 (d) and EST 200 (e). The arrows indicate that FBP 2000 and EST 512 have the highest image quality, while FBP 512 exhibits high noise, degraded features and blurred boundary of the tumour. A Hamming filter was used in the FBP reconstructions, while a non-local means filter was applied to the EST reconstructions. The line profiles along the white dashed line of all four reconstruction slices are shown in (f).

In the previous results, a hamming filter was applied in all the FBP reconstruction while a Non-local filter was applied in all the EST reconstruction. To demonstrate that the high resolution and high contrast EST reconstructed images are resulted from the characteristics of the advanced reconstruction algorithm not the de-noising filter, we also applied same Non-local filter onto FBP reconstruction. Fig. 8 shows the image quality comparison between EST 512 and FBP 512. The Non-local filter was applied to both the EST and FBP reconstructions. Though with the same filter, the noise level in FBP 512 is still higher than EST512, and the fine features indicated by the white arrows were still blurred and hard to identify for FBP512 reconstruction. This result suggests that the improvement of the image resolution and contrast is mainly due to the EST method but not the Non-local means filter.

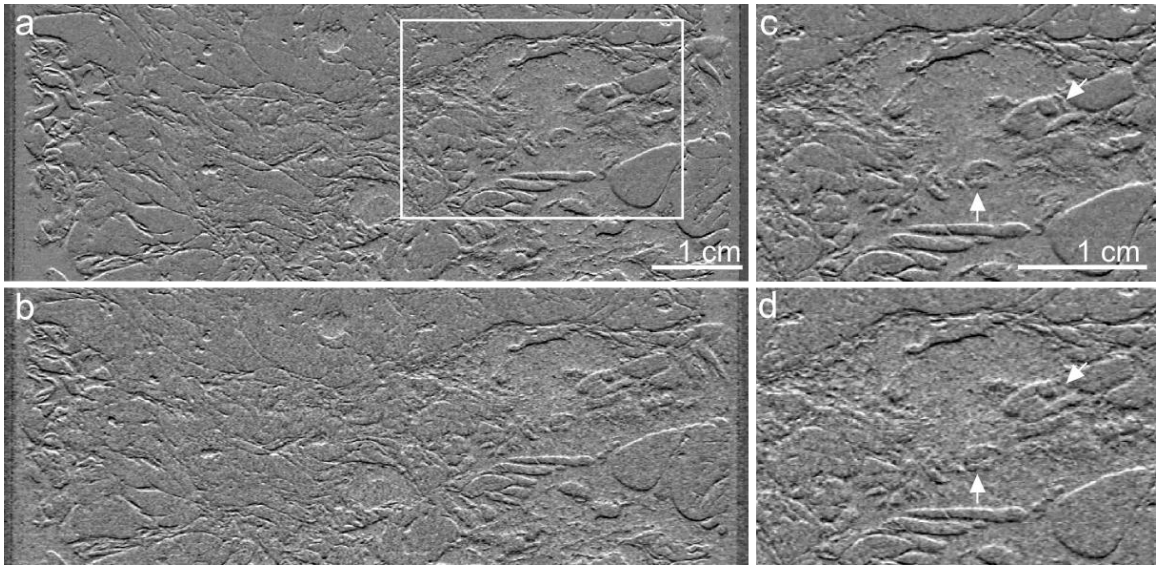

Figure 4.8. Reconstruction using EST and FBP with non-local means filter added with 512 projections. Image quality comparison between (**a**) EST 512 and (**b**) FBP 512. A non-local means filter was applied to both the EST and FBP reconstructions. Zoomed views of the tumour region by (**c**) EST 512 and (**d**) FBP 512. The white arrows indicate that, with the same non-local means filter, EST 512 shows more fine features in the tumour region than FBP 512.

4.3.2. Identification, segmentation and 3D visualization of tumour

The low dose and good quality PCT with EST reconstruction technique significant increase the capability of different tissue identification and tumour localization from the 3D reconstruction. A reformatted 92 μm thick sagittal slice and an axial slice from the EST 512 reconstruction are shown in Fig. 4.9. The fine details of the tumour, collagen strands, glandular tissue and fat are clearly resolved. Fig. 4.9 (b) and (d) shows a zoomed view of the tumour region, in which the

border of the tumour is distinctly visible and exhibits sharp edges. The partially discrete spiculations are a sign of malignancy in mammography.

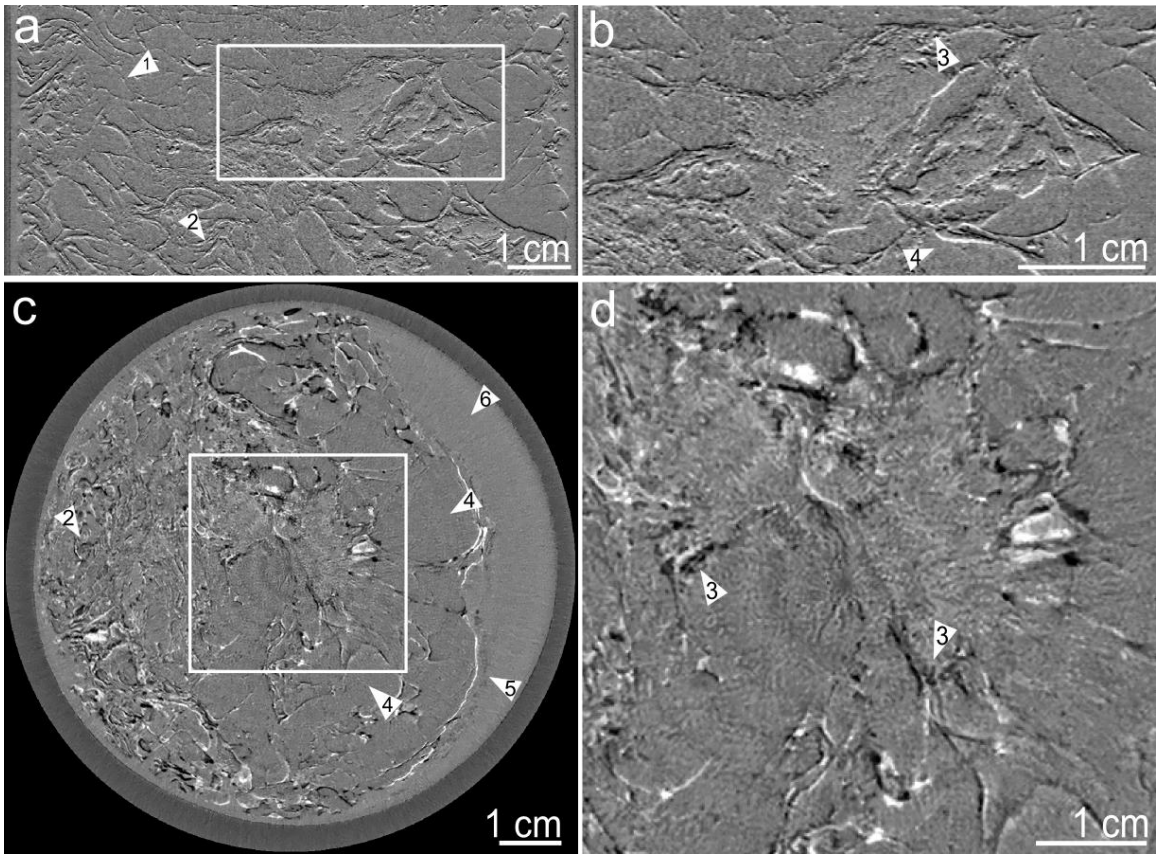

Figure 4.9. Identification of fine features in the tumour region and its surrounding tissues in the EST 512 reconstruction. (**a)**, A 92 μm thick sagittal slice (the rectangle indicates the tumour region). (**b)**, Zoomed view of the tumour region in the sagittal slice. (**c)**, A 92 μm thick axial slice (the square indicates the tumour region). (**d)**, Zoomed view of the tumour region in the axial slice. The arrows indicate various fine features in the EST 512 reconstruction: 1) collagen strands; 2) glandular tissue; 3) speculations; 4) fat; 5) skin; and 6) formalin.

Using the segmentation method described before, the 3D tumour segmentation volume is shown in Fig. 4.10. Fig. 4.10 (a) shows the segmented tumour in an axial slice, in which the yellow contour line indicates the tumour boundary. Three perpendicular slices of the segmentation are shown in Fig. 4.10 (b) and the whole 3D volume renderings are displayed in Fig. 4.10 (c). The 3D segmented tumour (in red) and its surrounding tissues such as skin, lobules and lactiferous duct are clearly visible, and the total volume of the elongated tumour was estimated to be ~2.7 cm^3. When rotating the 3D volume rendering result, a movie can be generated for better visualization and diagnosis purpose. Fig. 4.11 shows six snap shots from the movie, which shows the tumour in the breast sample from six different angles.

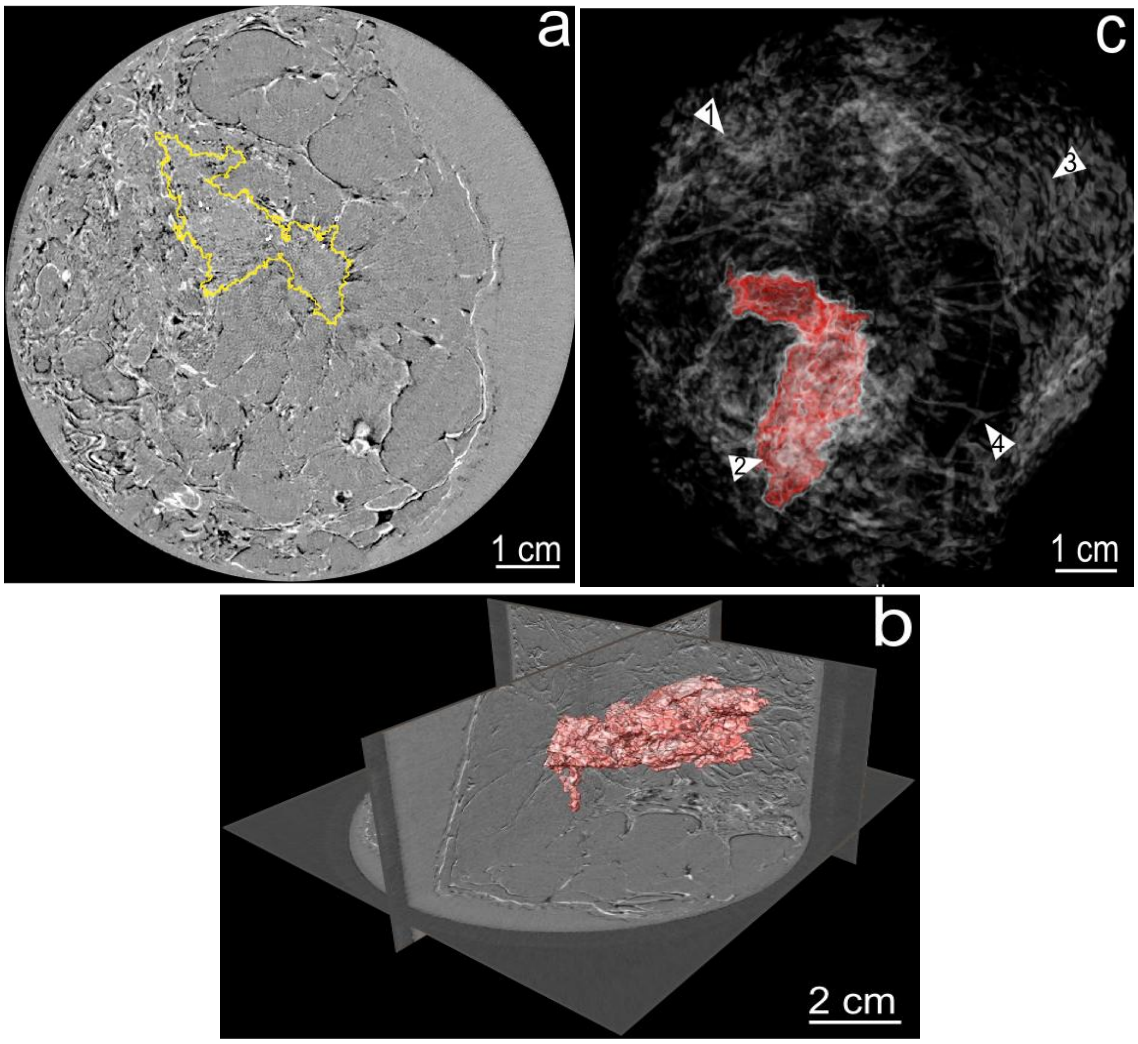

Figure 4.10. 3D visualization of the tumour from the EST 512 reconstruction. (**a)**, a segmented tumour in an axial slice, in which the yellow contour line indicates the tumour boundary. (**b)**, three perpendicular slices of the segmented tumour (in red). (**c)**, 3D volume renderings of the tumour (in red) in which the arrows indicate different fine features: 1) lobules; 2) tumour; 3) skin; and 4) lactiferous duct.

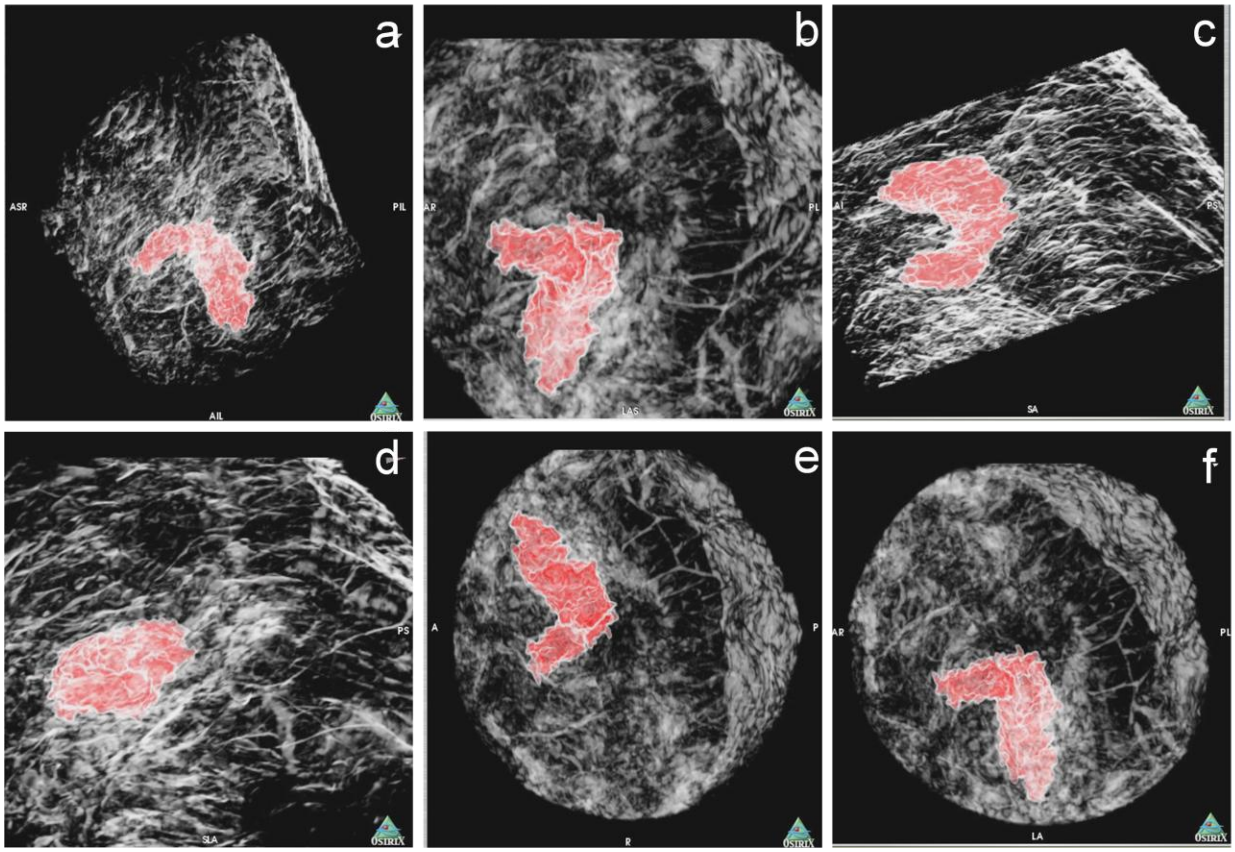

Figure 4.11. Snapshots from the 3D tumour visualization movie from the EST 512 reconstructions. After segmentation, the 3D tumour cell can be localized and identify clearly in the breast sample. The boundary of the tumour is separated from the other soft tissues.

4.3.3. Radiologist Blind Test

Table 4.1 summarizes the results of the experienced and independent radiologists' blind evaluation, suggesting that EST 512 outperforms FBP 2000 in all five categories. Furthermore, the EST 200 reconstruction is not only superior to FBP 512 (outperforms in 4 out of the total five categories), but also shows an image quality with fine structures that is still clinically acceptable.

	FBP 2000	**EST 512**	**FBP 512**	**EST 200**
Overall Image Quality	4.3 ±0.9	4.5 ±0.5	2.2 ±0.4	2.7 ±0.9
Sharpness	4.0 ±0.7	4.3 ±0.5	3.3 ±0.5	2.2 ±0.8
Image Contrast	4.0 ±0.5	4.8 ±0.4	3.0 ±0.7	3.4 ±1.0
Evaluation of Different Structure	4.1 ±0.6	4.8 ±0.4	2.6 ±0.5	2.9 ±1.0
Noise Level	4.2 ±0.6	4.8 ±0.3	1.8 ±0.8	3.3 ±0.8

Table 4.1. Results of a blind evaluation made by five independent, experienced radiologists. Two sets of images each consisting of the FBP 2000, EST 512, FBP 512 and EST 200 reconstructions were used in the evaluation based on five criteria: overall image quality, image sharpness, image quality, evaluation of different structure and noise level, where "5" means the best and "1" the worst. A Hamming filter was used in the FBP reconstructions, while a non-local means filter was applied to the EST reconstructions.

These visualization results along with the radiologists' evaluation and quantitative comparisons demonstrate that the EST method not only significantly reduces the number of projections relative to the standard FBP method, but also preserves the high resolution and sensitivity of PCT in discriminating the fine 3D structures and morphology of the tumour and soft tissues.

4.4. Discussions

The radiation dose for the FBP 2000 and EST 512 reconstructions was estimated based on the measurement using an ionization chamber installed on the biomedical beamline. The Mean Glandular Dose (MGD), calculated by Monte Carlo simulations (31), is 7.7 ± 0.1 mGy for the FBP 2000 reconstruction and 2.0 ± 0.1 mGy for the EST 512 reconstruction, indicating a radiation dose reduction of ~74%. Furthermore, according to the US Food and Drug Administration (FDA), the MGD of the U.S. dual-view screening mammography system was estimated to be ~3.0-3.52 mGy (32). This suggests that the combination of the EST method with PCT can not only provide high resolution and high contrast 3D diagnosis of human breast cancers, but also requires radiation doses less than that in dual-view screening mammography. According to the blind evaluation by five radiologists, while the overall image quality is lower than that of EST 512 and FBP 2000, EST 200 still outperforms FBP 512 and the 3D breast tumour structure remains visible. The total radiation dose in EST 200 is reduced to 0.8 ± 0.1 mGy, which is about four times lower than that in dual-view screening mammography.

Compared to the conventional PCT reconstruction (i.e. FBP), the EST method utilizes an iterative process to search for the missing information based on a limited number of projections and physical constraints, while keeping the reconstruction consistent with the experimental data. Furthermore, the EST method implemented in this study requires no interpolation in Fourier space, and is automatically terminated when a solution is reached. Because of the use of a fast Fourier transform in the iterative process, the computational time for the EST reconstruction of a 2048 x 2048 pixel slice (21 iterations) is about 1.4 minutes on a 2.66 GHz Intel Nehalem with 4GB of RAM computer. By combining this general reconstruction method with PCT, we not only achieved high contrast 3D imaging of a human breast cancer sample with a pixel size of 92 μm, but also reduced the radiation dose by ~74% relative to the standard FBP method. As importantly, the significant reduction of the number of projections also implies that the acquisition time can in principle be improved by a factor of ~74% (i.e. reduced from 25.1 to 6.6 minutes), which is another critical factor in pursuing *in-vivo* imaging and clinical application of PCT. Furthermore, if a slightly higher noise level is tolerable, the EST method can be applied to the screening and diagnosis of human breast cancers with an even lower radiation dose (~0.8 ± 0.1 mGy) and a faster acquisition time (~2.5 minutes).

In conclusion, we have demonstrated that, compared to current clinical mammography, the method reported here can not only provide the 3D information of soft tissues and tumours at higher resolution and better contrast, but also deliver less radiation doses to the sample. As compact x-ray sources and dedicated medical imaging beamlines are currently under rapid development worldwide (24, 33-37), this work represents an important step towards the clinical

application of PCT for 3D screening and diagnosis of human breast cancers. Finally, while in this study we used a human breast cancer sample as a proof of principle, this method can in principle be applied to other medical tomography fields where high resolution, high contrast, low radiation doses and fast data acquisition are crucially needed (28).

References

1. "World Cancer Report"(2008). International Agency for Research on Cancer.
2. Pisano, E.D., *et al*. (2005) Diagnostic performance of digital versus film mammography for breast-cancer screening. *N. Engl. J. Med.* 353, 1773-1783.
3. Brewer, N.T., Salz, T. & Lillie, S.E. (2007) Systematic review: the long-term effects of false-positive mammograms. *Ann. Intern. Med.* 146, 502–510.
4. Kolb, T.M., Lichy, J. & Newhouse, J.H. (2002) Comparison of the performance of screening mammography, physical examination, and breast US and evaluation of factors that influence them: An analysis of 27,825 patient evaluations. *Radiology* 225, 165–175.
5. Feig, S. & Hendrick, R. (1997) Radiation risk from screening mammography of women aged 40–49 years. *J. Natl. Cancer Inst. Monogr.* 22, 119–124.
6. Lindfors, K.K. *et al*. (2008) Dedicated breast CT: initial clinical experience. *Radiology* 246, 725-733.
7. Chantler, C.T. *et al*. (2005) X-Ray Form Factor, Attenuation and Scattering Tables (version 2.1): http://physics.nist.gov/ffast.

8. Fitzgerald, R. (2000) Phase-sensitive X-Ray imaging. *Phys. Today* 53, 23–27.
9. Momose, A., Takeda, T., Itai, Y. & Hirano, K. (1996) Phase-contrast X-ray computed tomography for observing biological soft tissues. *Nat. Med.* 2, 473-475.
10. Takeda, T. *et al*. (2000) Human Carcinoma: Early Experience with Phase-Contrast X-ray CT with Synchrotron Radiation—Comparative Specimen Study with Optical Microscopy. *Radiology* 214, 298-301.
11. Zhu, Z. *et al*. (2010) Low-dose, simple, and fast grating-based X-ray phase-contrast imaging. *Proc. Natl. Acad. Sci. USA* 107, 13576–13581.
12. Sztr6kay, A *et al* (2012) High-resolution breast tomography at high energy: a feasibility study of phase contrast imaging on a whole breast. *Phys. Med. Biol.* 57, 2931-2942.
13. Fitzgerald, R. (2000) Phase-sensitive X-Ray imaging. *Phys. Today* 53, 23–27.
14. Davis, T.J., Gao, D., Gureyev, T.E., Stevenson, A.W. & Wilkins, S.W. (1995) Phase-contrast imaging of weakly absorbing materials using hard X-rays. *Nature* 373, 595-598.
15. Snigirev, A., Snigireva, I., Kohn, V., Kuznetsov, S. & Schelokov, I. (1995) On the possibilities of x-ray phase contrast microimaging by coherent high-energy synchrotron radiation. *Rev. Sci. Instrum.* 66, 5486-5492.
16. Wilkins, S.W., Gureyev, T.E., Gao, D., Pogany, A. & Stevenson, A.W. (1996) Phase-contrast imaging using polychromatic hard X-rays. *Nature* 384, 335 - 338.
17. Chapman, D. *et al*. (1997) Diffraction enhanced x-ray imaging. *Phys. Med. Biol.* 42, 2015-2025.
18. Pfeiffer, F., Weitkamp, T., Bunk, O. & David, C. (2006) Phase retrieval and differential phase-contrast imaging with low-brilliance X-ray sources. *Nat. Phys.* 2, 258-261.

19. Miao, J., Föster, F. & Levi, O. (2005) Equally sloped tomography with oversampling reconstruction. *Phys. Rev. B* 72, 052103.

20. Lee, E. *et al*. (2008) Radiation dose reduction and image enhancement in biological imaging through equally sloped tomography. *J. Struct. Biol.* 164, 221–227.

21. Fahimian, B.P., Mao, Y., Cloetens, P. & Miao, J. (2010) Low dose X-ray phase-contrast and absorption CT using equally-sloped tomography. *Phys. Med. Biol.* 55, 5383-5400.

22. Mao, Y., Fahimian, B.P., Osher, S.J. & Miao, J. (2010) Development and optimization of regularized tomographic reconstruction algorithms utilizing equally-sloped tomography. *IEEE Trans. Image Processing* 19, 1259-1268.

23. Scott, M. C. *et al*. (2012) Electron tomography at 2.4 Ångstrom resolution. *Nature* 483, 444-447..

24. Bravin, A. *et al*. (2007) High-resolution CT by diffraction-enhanced x-ray imaging: mapping of breast tissue samples and comparison with their histo-pathology. *Phys. Med. Biol.* 52, 2197–2211.

25. Coan, P. et al. (2006) Evaluation of imaging performance of a taper optics CCD 'FReLoN' camera designed for medical imaging. *J. Synch. Rad*. 13, 260-270.

26. Diemoz, P.C., Bravin, A. Glaser, C. Coan P. (2010) Comparison of analyzer-based imaging computed tomography extraction algorithms and application to bone-cartilage imaging. *Phys. Med. Biol.* 55, 7663-7679.

27. Buades, A., Coll, B. & Morel, J.M. (2005) A review of image denoising algorithms with a new one. *Multiscale Model Simul.* 4, 490-530.

28. Kak, A.C. & Slaney, M. (2001) in *Principles of Computerized Tomographic Imaging.* (SIAM, Philadelphia, PA).

29. Li, Y. et al. (2010) A review of methods of clinical image quality evaluation in mammography. *Eur. J. Radiol*. 74, e122-31.

30. Vachier, C. & Meyer, F. (2005) The Viscous Watershed Transform. *J. Math. Imaging and Vis.* 22, 251-267.

31. Strulab, D., Santin, G., Lazaro, D., Breton, V. & Morel, C. (2003) GATE (geant4 application for tomographic emission): a PET/SPECT general-purpose simulation platform. *Nucl. Phys. B (Proc. Suppl.)* 125, 75-79.

32. Health Center for Devices and Radiological Center, National Statistics (MQSA), (2003) Dose and Image Quality in Mammography: Trends during the First Decade of MQSA (http://www.fda.gov/Radiation-EmittingProducts/

33. MammographyQualityStandardsActandProgram/FacilityScorecard/ucm113606.htm) .

34. Carroll, F.E., Mendenhall, M.H., Traeger, R.H., Brau, C. & Waters, J.W. (2003) Pulsed tunable monochromatic x-ray beams from a compact source: new opportunities. *Am. J. Roentgenol*. 181, 1197–1202.

35. Tuohimaa, T., Otendal, M. & Hertz, H.M. (2007) Phase contrast x-ray imaging with a liquid-metal jet-anode microfocus source. *Appl. Phys. Lett.* 91, 074104.

36. Castelli, E. *et al*. (2007) Clinical mammography at the SYRMEP beam line. *Nucl. Instrum. Meth. A* 572, 237–240.

37. Schlenvoigt, H.P. *et al.* (2008) A compact synchrotron radiation source driven by a laser-plasma wakefield accelerator, *Nat. Phys.* 4, 130-133.

38. Kneip, S. *et al*. (2010) Bright spatially coherent synchrotron X-rays from a table-top source. *Nat. Phys.* 6, 980–983.